Dynamics of Buoyancy-Driven Viscous Drops in Constricted Capillaries Including Effects of Soluble Surfactants

by

Ufuk Olgaç

A Thesis Submitted to the

Graduate School of Engineering

in Partial Fulfillment of the Requirements for

the Degree of

Master of Science

in

Mechanical Engineering

Koç University

November, 2005

Koç University

Graduate School of Sciences and Engineering

This is to certify that I have examined this copy of a master's thesis by

Ufuk Olgaç

and have found that it is complete and satisfactory in all respects,
and that any and all revisions required by the final
examining committee have been made.

Committee Members:

_____

Assistant Prof. Metin Muradoğlu (Advisor)

_____

Prof. Burak Erman

_____

Assistant Prof. Murat Sözer

Date: _____

ABSTRACT

Buoyancy-driven motion and breakup of viscous drops in sinusoidally constricted channels including the effects of soluble surfactants are studied computationally using a Finite-Volume/Front-Tracking (FV/FT) method. Computational results are first compared with the available experimental data and then the conditions for a drop breakup are examined. The effects of the channel geometry, drop size, Bond number and surfactant concentration on drop breakup are investigated. It is found that the present computational results are in a good agreement with the available experimental data and drop breakup occurs in various modes depending on the channel geometry, the relative drop size, Bond number and surfactant concentration. It is observed that a drop breaks up into two or more drops when its size is larger than a critical value. It is also found that large drops undergo successive breakups to produce mono-dispersed small droplets. Critical non-dimensional drop size and critical capillary number for the onset of drop breakup are reported over a wide range of geometrical parameters and Bond numbers.

Keywords: Buoyancy-driven motion; drop breakup; constricted channel; finite-volume/front-tracking method; surfactant.

ACKNOWLEDGMENTS

TABLE OF CONTENTS

LIST OF TABLES

LIST OF FIGURES

x

NOMENCLATURE

A	amplitude of corrugation
α	channel constriction parameter
ADI	Alternating Direction Implicit
Bi	Biot number
Bo	Bond number
C	bulk surfactant concentration
Ca	Capillary number
cov	surfactant coverage
d	drop diameter
D_s	diffusion coefficient
Δt	real-time step
$\Delta\rho$	density difference between the drop and the ambient fluids
$\Delta\tau$	pseudo-time step
η	nondimensional corrugation wavelength
FV-FT	Finite Volume-Front Tracking
Γ	surfactant concentration
Γ_{eq}	equilibrium surfactant concentration
Γ_{inf}	maximum possible surfactant concentration
γ	ratio of the drop to the ambient fluid densities
g_z	gravitational acceleration
h	wavelength of corrugation
H	channel height
κ	dimensionless drop size
κ_{cr}	dimensionless critical drop size
κ_c	twice of the mean curvature

L	length scale
λ	ratio of the drop to ambient fluid viscosities
Λ	ratio of the channel radius at throat to the drop radius
μ_d	viscosity of the drop
μ_o	viscosity of the suspending fluid
ν	kinematic viscosity of the drop fluid
p	pressure
Pe	Peclet number
r and z	radial and axial coordinates
R	radius of the tube
R_{break}	radius of the neck for the onset of breakup
R_d	radius of the drop
R_{th}	radius of the tube at the throat
Re	Buoyancy Reynolds number
ρ_o	density of the ambient fluid
ρ_d	density of the drop
σ	surface tension coefficient
t	physical time
T	time scale
τ	pseudo time
τ_{rr}, τ_{zz} and τ_{zr}	viscous stresses
U_m	nondimensional average rise velocity
V	velocity scale
v_r and v_z	velocity components in r and z coordinate directions
$\mathbf{x}_f$	location of the front

Chapter 1

INTRODUCTION

The motion and breakup of deformable drops and bubbles through constant and variable cross-section capillaries are of fundamental importance as a prototype problem in many engineering and scientific applications and natural processes. Examples include the microfluidic systems [10], oil recovery by chemical flooding [7, 19], and chemical and biological processes [3, 8, 9, 22]. In oil recovery systems, oil trapped in the porous matrix of underground reservoirs is displaced by flowing an aqueous liquid or a gaseous foam through the medium, forcing the trapped oil toward a collection well. Using foams as a means of sweeping out a porous material of either oil or another liquid is a useful process [12]. The fundamental mechanism associated with the formation of a foam in porous media is called snap-off and this process was identified by Roof as the primary mechanism in the breakup of a droplet as it travels through a porous media [28]. Hence, evaluating enhanced recovery methods critically depends on understanding the dynamics of drops and bubbles through porous media. For this reason, straight cylindrical capillaries were used extensively as a pore-scale model in early studies [7, 18]. However, in many engineering and scientific applications, the individual pores or channels are tortuous with rapid changes in the local cross-sectional area. To include this feature, the constricted channels have been proposed as prototype pore-scale models [5, 6, 7, 16]. In particular, periodically constricted capillary has attracted considerable interest since it renders the flow unsteady in a Lagrangian sense with the reproduction of certain features of the flow kinematics, which can have significant influence on the mobility of the drop and drop breakup [5, 6, 7].

Surfactants also play an important role on the dynamics of drops and bubbles in capillaries. They are either present as impurities or are deliberately added to the fluid mixtures to reduce the surface tension. Presence of surface-active impurities can lead to variations of interfacial tension across free-surfaces. It is well-established that such interfacial tension

gradients lead to tangential stresses which affect the motion of the fluid-fluid interface [30]. In oil recovery systems, surfactants are used as an aid in the formation of foams in porous media as they can enhance the breakup of droplets and bubbles [26]. However, in some cases, their presence is not positive, but they are difficult to remove from the system. Hence, the effects of surfactants should be properly understood for the results of fundamental problems to be useful in real engineering applications.

In the context of this thesis, the most relevant experimental studies on the motion of drops in capillaries have been performed by Olbricht and Leal [6], Hemmat and Borhan [5] and Almatroushi and Borhan [17]. Olbricht and Leal [6] considered the motion of immiscible neutrally-buoyant drops in pressure-driven flow through a horizontal capillary whose diameter varies periodically with axial position. They measured the average drop speed and correlated those values with the observed time-dependent drop shapes. Their results were mainly qualitative and demonstrated the effect of capillary geometry on the shape and mobility of drops. Hemmat and Borhan [5] reported the buoyancy-driven motion of viscous drops and gas bubbles through a vertical capillary with periodic constrictions in order to examine the effects of capillary geometry on drop deformation and breakup. Almatroushi and Borhan [17] studied the effects of surfactant on the buoyancy-driven motion of bubbles and drops in a tube. They reported the terminal rise velocities of fluid particles and their steady shapes for various bulk-phase concentrations of surfactant. Some of the experimental cases studied by Hemmat and Borhan [5] and Almatroushi and Borhan [17] are used in the present work to validate the computational results.

On the theoretical and computational side, the previous studies have been mostly restricted to the straight cylindrical or polygonal capillaries with uniform cross-sectional areas as reviewed by Olbricht [7]. However, a number of theoretical and computational investigations of the motion and breakup of drops and bubbles in variable cross-section channels have been also reported, for example, by Westborg and Hassanger [27], Gauglitz and Radke [16] and Tsai and Miksis [12, 26] but almost all in the limiting case of creeping flow regime. In constricted channels, flow is inherently unsteady and inertial effects are usually important. Especially in the case of small capillary numbers or severely constricted channels, the finite Reynolds number effects must be taken into account [7]. Recently Muradoglu and Gokaltun [20] have studied the motion of two-dimensional buoyancy-driven drops through

sinusoidally constricted channels with finite Reynolds numbers but have not reported any drop breakup in the cases they studied. Drop breakup is of fundamental importance as it is the key process that determines the critical conditions for the existence of steady drop shapes and the final drop distribution in a multiphase system [22].

Most of the previous numerical studies on the effects of surfactants pertain to extensional flows. Stone and Leal [23] investigated the effects of insoluble surfactants on the deformation and breakup of drops. They determined that the degree of deformation is influenced by the accumulation of surfactant at the ends of the drop which is caused by the external flow, i.e., uniaxial extension in their case. Milleken et al. [24] generalized their work for a range of drop fluid viscosities and a nonlinear equation of state for the interfacial tension. They found that surfactants facilitate the formation of pointed ends during drop stretching, and attributed this as the reason for tip-streaming observed in experiments. More recently, Eggleton et al. [25] used boundary integral methods to investigate the onset of tip-streaming again for linear extensional flow. They found that, similar to Stone and Leal [23], surfactant is accumulated at the drop poles where it drives the surface tension to near zero. They observed that the drop assumes a transient shape with highly pointed tips from which thin liquid threads are pulled. If the initial coverage value is high enough, this may lead to breakup with tail-streaming mode.

The thesis is organized as follows. In the next chapter, the mathematical formulation and the numerical method is described. Computations are performed using a finite-volume/front-tracking method developed by Muradoglu and Kayaalp [21]. The governing equations for axisymmetric geometry are solved numerically on a curvilinear grid using a finite-volume method. The drop interface is represented by connected Lagrangian marker points which move with the local flow velocity. The flow equations are written for the entire computational domain and different phases are treated as single fluid with variable material properties. The effects of the surface tension are taken into account by treating them as body forces in the same way as described by Unverdi and Tryggvason [13]. In Chapter 3, the motion and breakup of axisymmetrical buoyancy-driven viscous drops through sinusoidally constricted capillaries is considered which was studied experimentally by Hemmat and Borhan[5]. It is found that the present computational results are in a good agreement with the available experimental data. Then the method is used to study the effects of the

drop size, the channel geometry and Bond number on the motion and breakup of viscous drops in constricted capillaries. It is shown that a viscous drop breaks up into smaller drops when the non-dimensional drop size exceeds a critical value as was experimentally observed by Hemmat and Borhan [5]. The breakup is usually initiated with the retarding effect of the constrictions. When a drop is passing through a constriction, as the leading edge clears off the constriction, its velocity begins to rise while the trailing edge is trapped behind the constriction, which causes formation of a neck and eventually leads to a breakup of the drop if the drop size is sufficiently large, i.e., it is larger than a critical value. It is also found that different modes of breakup occur at various Bond numbers and channel geometries. Although it is widely believed that tail streaming occurs due to accumulation of surfactant [14, 15], a breakup mode is observed that resembles the tail streaming in surfactant free cases as well. In Chapter 4, the effects of surfactants on the dynamics of buoyancy-driven viscous drops are investigated which was studied experimentally by Almatroushi and Borhan [17]. The computational results are found to have the same trend with the experimental data. It is observed that the average rise velocity of large drops considerably increases with increasing surfactant concentrations as also observed by Almatroushi and Borhan [17]. It is also seen that surfactant enhances breakup and tail-streaming as reported by Borhan and Pallinti [14, 15], Tsai and Miksis [26] and Eggleton et al. [25]. Addition of surfactants decreases the critical nondimensional drop size for the onset of breakup. Finally, some conclusions are drawn in Chapter 5.

<div align="center">

Chapter 2

NUMERICAL METHOD

</div>

In this chapter, the governing equations are briefly reviewed and transformed into an arbitrary curvilinear coordinate system. Then the finite-volume/front-tracking algorithm is described in detail.

2.1 Mathematical Formulation

The incompressible flow equations for an axisymmetric flow can be written in the cylindrical coordinates in the vector form as

$$\frac{\partial \mathbf{q}}{\partial t} + \frac{\partial \mathbf{f}}{\partial r} + \frac{\partial \mathbf{g}}{\partial z} = \frac{\partial \mathbf{f}_v}{\partial r} + \frac{\partial \mathbf{g}_v}{\partial z} + \mathbf{h}_v + \mathbf{f}_b, \tag{2.1}$$

where

$$\mathbf{q} = \left\{ \begin{array}{c} 0 \\ r\rho v_r \\ r\rho v_z \end{array} \right\}, \quad \mathbf{f} = \left\{ \begin{array}{c} rv_r \\ r(\rho v_r^2 + p) \\ r\rho v_r v_z \end{array} \right\}, \quad \mathbf{g} = \left\{ \begin{array}{c} rv_z \\ r\rho v_r v_z \\ r(\rho v_z^2 + p) \end{array} \right\}, \tag{2.2}$$

and

$$\mathbf{f}_v = \left\{ \begin{array}{c} 0 \\ \tau_{rr} \\ \tau_{zr} \end{array} \right\}, \quad \mathbf{g}_v = \left\{ \begin{array}{c} 0 \\ \tau_{zr} \\ \tau_{zz} \end{array} \right\}, \quad \mathbf{h}_v = \left\{ \begin{array}{c} 0 \\ p - \frac{2}{r}\frac{\partial}{\partial r}(r\mu v_r) - \frac{\partial}{\partial z}(\mu v_z) \\ -\frac{\partial}{\partial z}(\mu v_z) \end{array} \right\}. \tag{2.3}$$

In Eqs.(2.1)-(2.3), r and z are the radial and axial coordinates and t is the physical time; ρ, μ and p are the fluid density, the dynamic viscosity and pressure; v_r and v_z are the velocity components in r and z coordinate directions, respectively. The elements of the viscous stresses appearing in the viscous flux vectors are given by

$$\tau_{rr} = 2\mu \frac{\partial(rv_r)}{\partial r}, \quad \tau_{zz} = 2\mu \frac{\partial(rv_z)}{\partial z}, \quad \tau_{zr} = \mu \left(\frac{\partial(rv_r)}{\partial z} + \frac{\partial(rv_z)}{\partial r} \right). \tag{2.4}$$

The last term in Eq.(2.1) represents the body forces resulting from the buoyancy and surface tension and is given by

$$\mathbf{f}_b = -r(\rho_o - \rho)\mathbf{G} - \int_S r\sigma\kappa\mathbf{n}\delta(\mathbf{x} - \mathbf{x}^f)ds, \tag{2.5}$$

where the first term represents the body force due to buoyancy with ρ_o and $\mathbf{G}$ being the density of ambient fluid and the gravitational acceleration, respectively. The second term in Eq.(2.5) represents the body force due to the surface tension, and δ, $\mathbf{x}_f$, σ, κ_c, $\mathbf{n}$, S and ds denote the Dirac delta function, the location of the front, the surface tension coefficient, the twice of the mean curvature, the outward unit normal vector on the interface, the surface area of the interface and the surface area element of the interface, respectively.

In Eq.(2.1), the fluids are assumed to be incompressible so that the density of a fluid particle remains constant, i.e.,

$$\frac{D\rho}{Dt} = 0, \tag{2.6}$$

where the substantial derivative is defined as $\frac{D}{Dt} = \frac{\partial}{\partial t} + \mathbf{u} \cdot \nabla$. It is also assumed that the viscosity in each fluid particle remains constant

$$\frac{D\mu}{Dt} = 0. \tag{2.7}$$

As can be seen in Eq.(2.1), the continuity equation is decoupled from the momentum equations since it does not have any time derivative term. In order to overcome this difficulty and to be able to use a time-marching solution algorithm, artificial time derivative terms are added to the flow equations in the form

$$\Gamma^{-1}\frac{\partial \mathbf{w}}{\partial \tau} + \mathbf{I}^1\frac{\partial \rho\mathbf{w}}{\partial t} + \frac{\partial \mathbf{f}}{\partial r} + \frac{\partial \mathbf{g}}{\partial z} = \frac{\partial \mathbf{f}_v}{\partial r} + \frac{\partial \mathbf{g}_v}{\partial z} + \mathbf{h}_v + \mathbf{f}_b \tag{2.8}$$

where τ is the pseudo time. The solution vector $\mathbf{w}$, the incomplete identity matrix I^1 and the preconditioning matrix Γ^{-1} are given by

$$\mathbf{w} = \left\{ \begin{array}{c} rp \\ rv_r \\ rv_z \end{array} \right\}, \quad I^1 = \left[\begin{array}{ccc} 0 & 0 & 0 \\ 0 & 1 & 0 \\ 0 & 0 & 1 \end{array} \right], \quad \Gamma^{-1} = \left[\begin{array}{ccc} \frac{1}{\rho\beta_c^2} & 0 & 0 \\ 0 & \rho & 0 \\ 0 & 0 & \rho \end{array} \right], \tag{2.9}$$

where β_c is the preconditioning parameter with dimensions of velocity [21].

With the goal of treating complex geometries, Eq.(2.8) can be transformed into a general, curvilinear coordinate system

$$\xi = \xi(r, z), \quad \eta = \eta(r, z), \tag{2.10}$$

and the resulting equations take the form

$$\Gamma^{-1}\frac{\partial h\mathbf{w}}{\partial \tau} + \mathbf{I}^1\frac{\partial \rho h\mathbf{w}}{\partial t} + \frac{\partial h\mathbf{F}}{\partial \xi} + \frac{\partial h\mathbf{G}}{\partial \eta} = \frac{\partial h\mathbf{F}_v}{\partial \xi} + \frac{\partial h\mathbf{G}_v}{\partial \eta} + h(\mathbf{h}_v + \mathbf{f}_b), \tag{2.11}$$

where

$$h = r_\xi z_\eta - r_\eta z_\xi, \tag{2.12}$$

represents the Jacobian of the transformation. The vectors

$$h\mathbf{F} = z_\eta \mathbf{f} - r_\eta \mathbf{g}; \quad h\mathbf{G} = -z_\xi \mathbf{f} + r_\xi \mathbf{g}, \tag{2.13}$$

and

$$h\mathbf{F}_v = z_\eta \mathbf{f}_v - r_\eta \mathbf{g}_v; \quad h\mathbf{G}_v = -z_\xi \mathbf{f}_v + r_\xi \mathbf{g}_v, \tag{2.14}$$

represent the transformed inviscid and viscous flux vectors, respectively.

The governing equations (Eq.(2.11) are solved using the finite-volume/front-tracking method developed by Muradoglu and Kayaalp [21]. The method combines a finite-volume solver with the front-tracking method developed by Unverdi and Tryggvason [13]. In this method, the spatial derivatives are discretized using a finite-volume method that is equivalent to a second order finite-differences on a uniform Cartesian mesh. Time integration in pseudo time is achieved by an alternating direction implicit (ADI) method [2]. Fourth-order numerical dissipation terms are added to the discrete version of the flow equations in the form described by Caughey [1] to prevent the odd-even decoupling. Several convergence acceleration techniques including the local time-stepping, preconditioning and multigrid methods are used to accelerate the convergence rate of the ADI method in pseudo time. A three point second order backward implicit method is used to approximate the physical time derivatives.

Three types of grids used in the present method are sketched in Fig. 2.1. Conservation equations are solved on a body-fitted curvilinear grid and the interface is represented by connected Lagrangian marker points moving with the local flow velocity interpolated from the neighboring grid points. A piece of the interface between two neighboring marker points is called a front element. The communication between the curvilinear grid and the interface marker points is maintained efficiently using an auxiliary Cartesian grid cast on the curvilinear grid as shown in Fig. 2.1. The material properties inside and outside of the drop are set based on the indicator function defined such that it is unity inside the droplet and zero outside. The indicator function is computed on the regular Cartesian grid using the procedure described by Tryggvason et al. [11] and then it is interpolated on the curvilinear
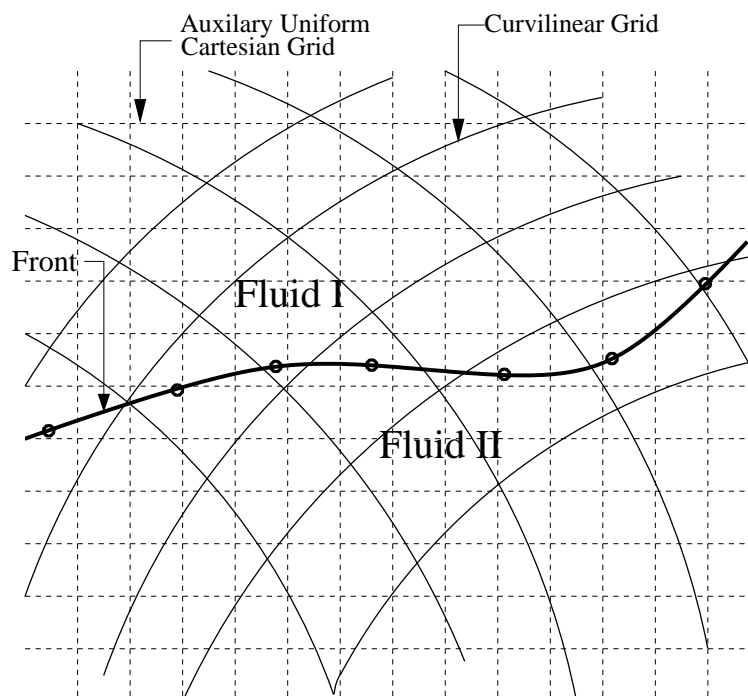
Figure 2.1: Three types of grids used in the computations. The governing equations are solved on a fixed Eulerian curvilinear grid and the interface between different phases is represented by a Lagrangian grid consisting of connected marker points. An auxiliary uniform Cartesian grid is used to maintain communication between the curvilinear and Lagrangian grids.

grid using bilinear interpolations. The interface marker points are also used to compute the surface tension forces at the interface which are then distributed on the neighboring curvilinear grid cells as body forces in a conservative manner. The details of the FV/FT method can be found in the references [20, 21]. Tracking algorithm is shortly described in the next section.

2.2   Tracking Algorithm

The interface between different phases are represented by a Lagrangian grid with connected marker points as shown in Fig. 2.1. The marker points can be considered as fluid particles moving with local flow velocity. In order to maintain communication between the Lagrangian and fixed curvilinear grids, it is necessary to determine the locations of the marker points in the curvilinear grid at every physical time step. For this purpose, the present

tracking algorithm utilizes an auxiliary uniform Cartesian grid as sketched in Fig. 2.1. The overall algorithm can be summarized as follows: At the beginning of each simulation, a uniform Cartesian grid is generated such that it covers the entire computational domain. The cell size of the uniform grid is typically taken as the half of the size of the smallest curvilinear grid cell. It is then found which uniform Cartesian grid nodes reside in each curvilinear grid cell and this information is stored in an array. Referring to the sketch in Fig. 2.2, for example, the nodal point Q is found to be in the curvilinear grid cell $ABCD$ by performing the vector operations $\vec{k} \cdot (|\overrightarrow{AB}| \times |\overrightarrow{AQ}|) \geq 0$, $\vec{k} \cdot (|\overrightarrow{BC}| \times |\overrightarrow{BQ}|) \geq 0$, $\vec{k} \cdot (|\overrightarrow{CD}| \times |\overrightarrow{CQ}|) \geq 0$, and $\vec{k} \cdot (|\overrightarrow{DA}| \times |\overrightarrow{DQ}|) \geq 0$, where $\vec{k}$ is the outward unit vector perpendicular to the cell $ABCD$. The same procedure is used for all other nodal points enclosed by the rectangle consisting of the uniform grid cells that enclose $ABCD$, i.e., the uniform grid cells in the rectangle shown by thick solid borderline in the sketch, and the entire process is repeated for all other curvilinear grid cells. It is emphasized that all these computations are done only once at the beginning of each simulation as a preprocessing. Then, in each physical time step, it is first determined where the front points reside in the uniform grid. Referring to the sketch in Fig. 2.3, for instance, it is first found that the front point P is in (I, J) cell of the uniform grid and then it is determined that the nodes of (I, J) cell reside in the curvilinear grid cells (i, j), $(i, j-1)$ and $(i-1, j-1)$ as shown by the dashed line in the sketch. As a result, we conclude that the front point P resides in the region consisting of the curvilinear grid cells $(i-1 : i, j-1 : j)$ and this region is expanded to include the cells $(i-2 : i+1, j-2 : j+1)$. Finally the cells $(i-2 : i+1, j-2)$ and $(i-2, j-2 : j+1)$ are eliminated based on the relative distance of their outer nodes to the point P compared to the cells $(i-2 : i+1, j+1)$ and $(i+1, j-2 : j+1)$, respectively. At the end of this process, it is determined that the front point P resides in the domain composed by the cells $(i-1 : i+1, j-1 : j+1)$. The front properties evaluated at the point P are distributed onto these cells and flow variables such as velocity field are interpolated onto point P from these cells. This tracking algorithm reduces the particle tracking in curvilinear grid to a particle tracking on a uniform grid with a look up table.
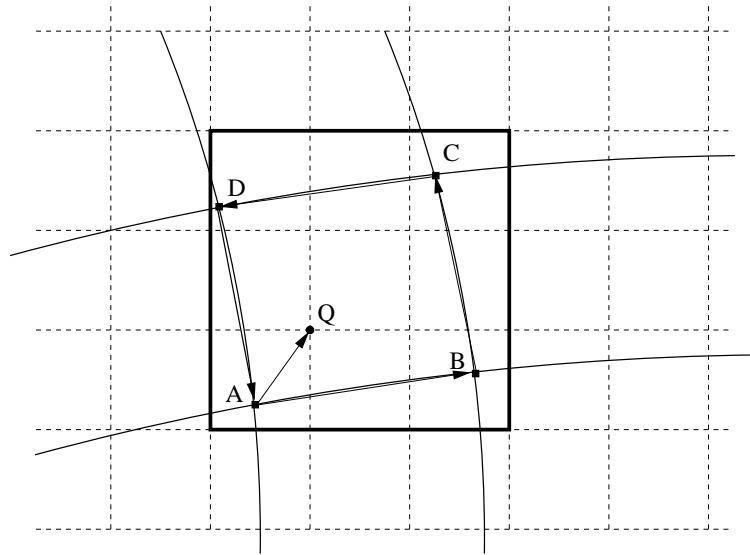
Figure 2.2: Preprocessing of the uniform Cartesian grid. Vector algebra is used to determine which uniform Cartesian grid nodes reside in each curvilinear grid cell.
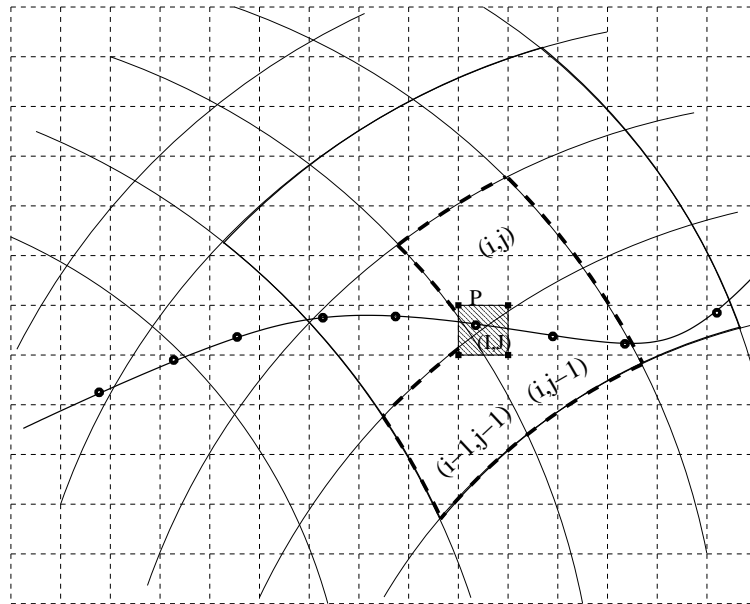
Figure 2.3: The tracking algorithm for curvilinear grids.

2.3 Treatment of Drop Breakup

It is assumed that a drop breakup occurs when the radius at the neck is smaller than a prespecified threshold value, R_{break}. For this purpose, the radius at the neck is monitored during the computation and when the neck radius is smaller than R_{break}, the front element that is closest to the centerline at the neck is deleted. After that the marker points at both ends of the deleted element are projected on the centerline and new boundary elements are created as shown in the sketch in Fig. 2.4. The threshold value is taken as the smallest curvilinear grid size in the present computations and it is found that the results are not sensitive to the choice of the threshold value as long as it is of order of the local grid size. This simple treatment of breakup is found to be very robust and gives reasonably good results compared to the experimental data as discussed in the following chapter.
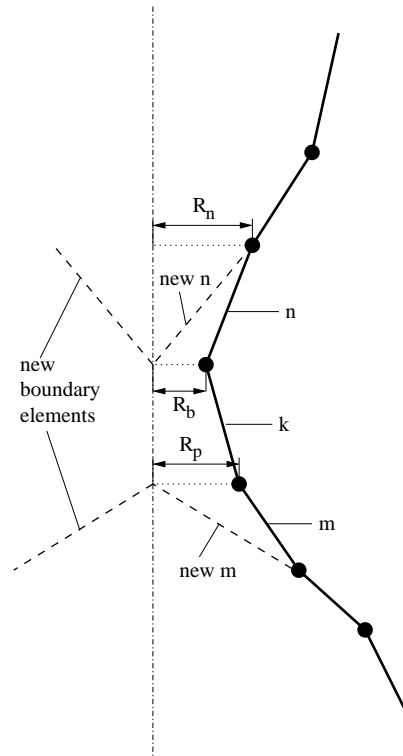
Figure 2.4: Treatment of a drop breakup. The front element k is deleted when R_b is smaller than a prespecified threshold value R_{break}, the marker points are projected on the centerline and new boundary elements are created as shown.

2.4   The Overall Solution Procedure

The finite-volume and front-tracking methods described above are combined as follows. In advancing solutions from physical time level n ($t_n = n \cdot \Delta t$) to level $n + 1$, the locations of the marker points at the new time level $n + 1$ are first predicted using an explicit Euler method, i.e.,

$$\widetilde{\mathbf{X}}_p^{n+1} = \mathbf{X}_p^n + \Delta t \mathbf{V}_p^n, \tag{2.15}$$

where $\mathbf{X}_p$ and $\mathbf{V}_p$ denote the position of front marker points and the velocity interpolated from the neighboring curvilinear grid points onto the front point $\mathbf{X}_p$, respectively. Then the material properties and surface tension are evaluated using the predicted front position as

$$\rho^{n+1} = \rho(\widetilde{\mathbf{X}}_p^{n+1}); \quad \mu^{n+1} = \mu(\widetilde{\mathbf{X}}_p^{n+1}); \quad \mathbf{f}_b^{n+1} = \mathbf{f}_b(\widetilde{\mathbf{X}}_p^{n+1}). \tag{2.16}$$

The velocity and pressure fields at new physical time level $n + 1$ are then computed by solving the flow equations (Eq. 2.13) by the FV method for a single physical time step and finally the positions of the front points are corrected as

$$\mathbf{X}_p^{n+1} = \mathbf{X}_p^n + \frac{\Delta t}{2}(\mathbf{V}_p^n + \mathbf{V}_p^{n+1}). \tag{2.17}$$

After this step the material properties and the body forces are re-evaluated using the corrected front position. The method is second order accurate both in time and space. All terms except $\mathbf{f}_b$ in Eq.(2.11) are treated implicitly in physical time so that the physical time is determined solely by the accuracy considerations and stability constraint mainly due to surface tension.

The Lagrangian grid is initially uniform and is kept nearly uniform throughout the computations by deleting small elements and splitting the large elements in the same way as described by Tryggvason et al. [11]. The initial front element size is typically set to $0.75\Delta l$, where Δl is the minimum size of the curvilinear grid cell. During the simulation, in each physical time step, the elements that are smaller than $0.5\Delta l$ are deleted and the elements that are larger than Δl are splited into two parts in order to keep the Lagrangian grid nearly uniform and to prevent the formation of wiggles much smaller than the grid size.

Chapter 3

BUOYANCY-DRIVEN MOTION AND BREAKUP OF VISCOUS DROPS IN CONSTRICTED CAPILLARIES*

The finite-volume/front-tracking method is first applied to the cases studied experimentally by Hemmat and Borhan [5] and then it is used to determine the conditions for the breakup of viscous drops in constricted capillaries.

The physical problem and the computational domain are sketched in Fig. 3.1a and a portion of a coarse curvilinear grid containing 8×416 grid cells is plotted in Fig. 3.1b to show the overall structure of the computational grid. Note that most of the computations are performed using finer versions of this grid, i.e., typically containing 32×1664 grid cells. In Fig. 3.1a, the left boundary is the axis of symmetry and all other boundaries are solid walls where no-slip boundary conditions are applied. The geometric parameters R, R_{th}, A, h and H represent the average capillary radius, the minimum capillary radius at throat, the corrugation amplitude, the corrugation wavelength and the channel height, respectively. A drop with diameter d and radius R_d is instantaneously placed in the ambient fluid that fully fills the cylindrical tube and is initially in the hydrostatic conditions. The drop is initially spherical if its initial radius is smaller than the radius of the capillary tube and is ellipsoidal otherwise. The drop radius d represents the equivalent drop diameter if the initial shape of the drop is not spherical. The drop has a viscosity μ_d and a density ρ_d while the ambient fluid has a viscosity μ_o and a density ρ_o. The drop starts rising due to buoyancy forces caused by the density difference $\Delta\rho = \rho_o - \rho_d$ and a constant gravitational acceleration denoted by $\mathbf{g}$. The viscosity and density ratios are defined as $\lambda = \mu_d/\mu_o$ and $\gamma = \rho_d/\rho_o$, respectively. The geometry of the channel is characterized by two non-dimensional parameters, namely, the ratio of the amplitude of corrugation to the average channel radius $\alpha = A/R$ and the ratio of the corrugation wavelength to the average channel radius $\eta = h/R$. The first parameter (α) characterizes the channel constriction level and is referred hereafter as the channel
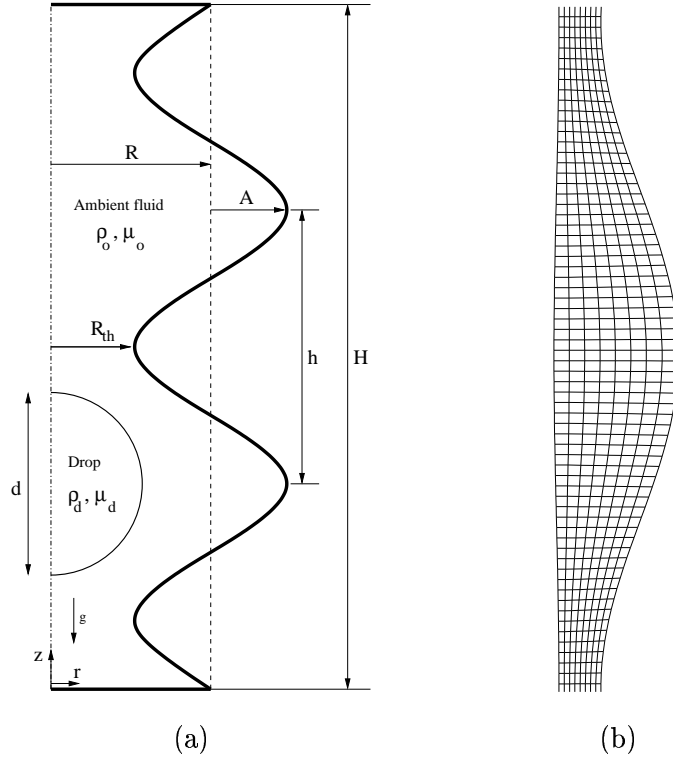
Figure 3.1: (a) Schematic illustration of the computational setup for a buoyancy-driven rising drop in a constricted channel for $\alpha = 0.50$. (b) A portion of a coarse computational grid containing 8×416 cells.

constriction parameter or simply constriction parameter while the second parameter (η) is the non-dimensional corrugation wavelength. The ratio of the channel at throat to the equivalent drop radius $\Lambda = R_{th}/R_d$ is also an important parameter that critically influences deformation and breakup of the drop. The non-dimensional drop radius is defined as the ratio of the equivalent spherical drop radius to the average capillary radius $\kappa = R_d/R$. The Bond number is defined as $Bo = \Delta\rho g R^2/\sigma$ representing the ratio of buoyancy forces to the interfacial forces.

The results are expressed in terms of non-dimensional quantities denoted by superscript "*". The dimensionless coordinates are defined as $z^* = z/h$ and $r^* = r/R$. Time and velocity are made dimensionless with the reference values of $T_{\text{ref}} = \frac{\mu_o}{\Delta\rho g R}$ and $V_{\text{ref}} = \frac{\Delta\rho g R^2}{\mu_o}$, respectively.

3.1 Comparison with Experimental Data

In the experimental setup [4, 5], the capillary tube consists of a 26 cm long, periodically constricted cylindrical tube with 6 corrugations. The internal radius of the capillary tube is $R = 0.5$ cm, the wavelength of the corrugations is $h = 4$ cm and the amplitude of the corrugations is $A = 0.07$ cm corresponding to the geometric parameters $\alpha = 0.14$ and $\eta = 8$. The suspending fluids are aqueous glycerol solutions (denoted by GW3 and GW5) and diethylene glycol-glycerol mixtures (denoted by DEGG10 and DEGG12). A variety of UCON oils are used as drop fluids. The properties of the drop and suspending fluids are summarized in Table 3.1 where the same label is used for each system as used by Hemmat and Borhan [5]. A complete description of the experimental set up can be found in [4, 5]. We consider four systems labeled as GW3, GW5, DEGG10 and DEGG12 (Table 3.1). It is emphasized here that, in addition to the reported measurement error up to 5% in the experimental data, there is inconsistency between the material properties and the non-dimensional numbers especially for DEGG12 system. For instance, the Bond number reported by Hemmat and Borhan [5] is about 10% larger than the value we computed directly from the given material properties and the average tube radius.

First a qualitative analysis for the evolution of the drop shapes is presented. For this purpose, sequences of images illustrating the evolution of the shapes of viscous drops as they move through the constricted channel are plotted in Fig. 3.2 for GW3, DEGG12 and GW5 systems with the non-dimensional drop sizes of $\kappa = 0.54$, 0.78 and 0.92. The computations are performed using a 32×1664 grid, the physical time step is $\Delta t^* = 1.641$ and the residuals are reduced by three orders of magnitude in each sub-iteration. It is emphasized that these numerical parameters result in less that a few percent of total numerical discretization error for all the quantities in the case of DEGG12 system shown in Fig. 3.2b and it is expected that the numerical error is about the same order for other cases. The readers are referred to the reference [21] for a detailed numerical error convergence analysis of the present finite-volume/front-tracking method. As can be seen in these figures, when a large drop ($\kappa > 0.7$) reaches a constriction, its leading edge follows the capillary wall contour and squeezes through the throat. Once the leading meniscus clears the throat, its rise velocity increases as it enters the diverging cross-section while the trailing edge of the drop remains trapped behind the throat. This behavior is in a very good agreement with the experimental

System	Suspending fluid	Drop fluid	μ_o (mPa·s)	μ_d (mPa·s)	ρ_o (kg/m^3)	ρ_d (kg/m^3)	σ (N/m)
GW3	glycerol-water (96.2wt%)	UCON-1145	450	530	1250	995	0.0105
GW5	glycerol-water (96.2wt%)	UCON-50HB100	450	97	1250	950	0.0057
DEGG10	diethylene-glycol (100.0wt%)	UCON-165	28	63	1110	975	0.0016
DEGG12	diethylene glycol-glycerol (63.8wt%)	UCON-285	87	115	1160	966	0.0042

Table 3.1: Two-phase systems used both in the experiments [4, 5] and in the present computations.

observations [5]. As the non-dimensional drop size gets larger, this necking may lead to a breakup of the drop as seen in Fig. 4c. The non-dimensional drop size for which the drop starts to break up is called the critical drop size and is denoted by κ_{cr}. For GW5 system, it is found computationally that the critical drop radius is about $\kappa_{cr} = 0.87$ which is very close to the experimental value of $\kappa_{cr} = 0.85$ [4, 5].

To better show the effects of the constrictions, the snapshots of the drops before and after the throat of the constriction are shown in Fig. 3.3 for GW3 system for drop sizes $\kappa = 0.54$, 0.65, 0.78, 0.85 and 0.92. No breakup is observed for GW3 system in this drop size range. A typical drop breakup is shown in Fig. 3.4. In this figure, the breakup process for a GW5 drop with the non-dimensional drop size of $\kappa = 0.90$ is illustrated through a series of snapshots taken just before and after the breakup. The evolutions and shapes of the drops shown in Figs. 3.3 and 3.4 qualitatively compare very well with the experimental observations [5]. In order to quantify the motion and evolution of drops as they pass through the corrugations, a deformation parameter denoted by D is defined as the ratio of the perimeter of the deformed drop profile to that of the equivalent spherical drop.

GW3

(a)

DEGG12

(b)

GW5

(c)
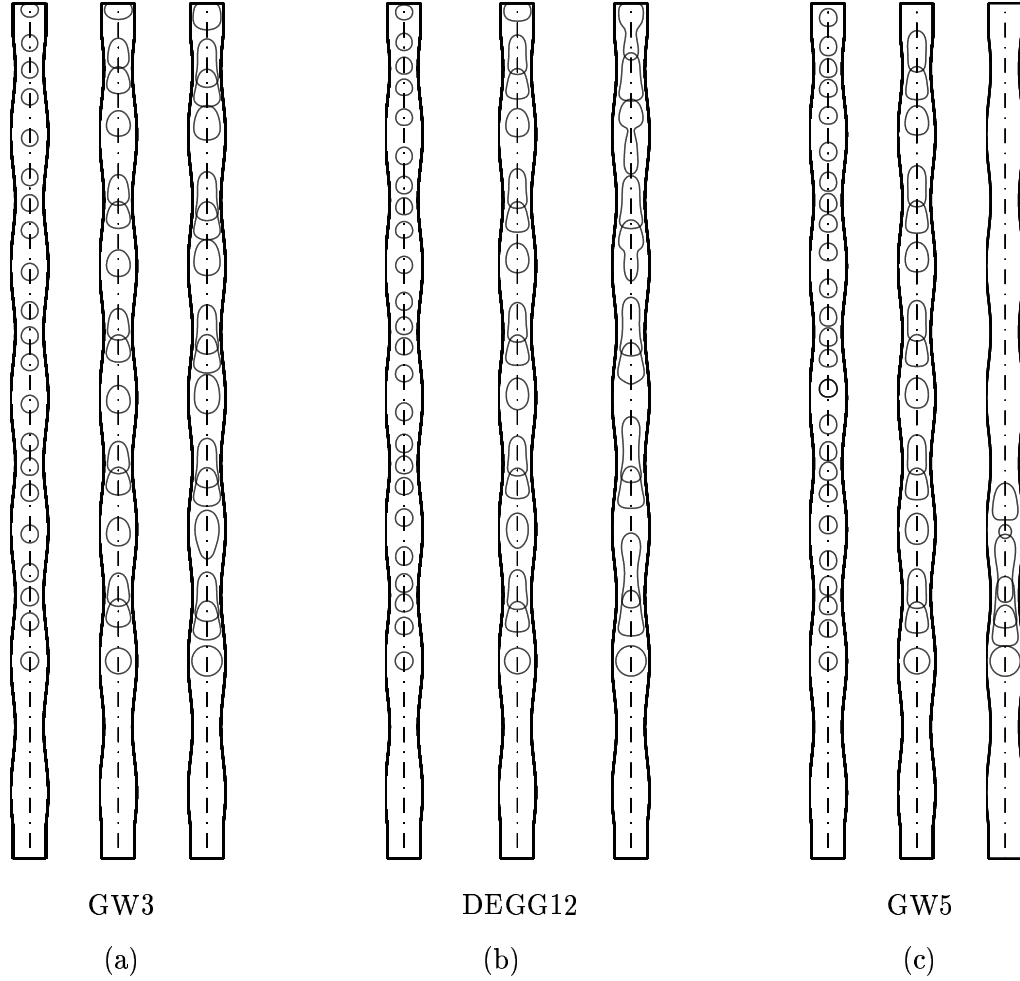
Figure 3.2: Snapshots of buoyant drops of (a) GW3 system, (b) DEGG12 system and (c) GW5 system for drops sizes $\kappa = 0.54$, 0.78 and 0.92 from left to right for each system. The gap between two successive drops in each column represents the distance the drop travels at a fixed time interval and the last interface is plotted from left to right at $t^* = $ (a) 1044.4, 783.3, 783.3 (b) 2831.3, 3693.0, 5416.4 (c) 1883.5, 1785.4 and 486.6, respectively.

In addition, the non-dimensional axial length of the drop is defined as the axial length of drop profile scaled by the wavelength of corrugation and is denoted by L. Both D and L are plotted in Fig. 3.5 together with the experimental data within one period of corrugation for various values of drops sizes of GW3 system. As can be seen in this figure, the general trends both for D and L are well captured by the present computations. The deformation is negligibly small for small drops, i.e., drops with $\kappa < 0.60$, and increases rapidly as the drop size gets larger. The discrepancy between the computed and the experimental results
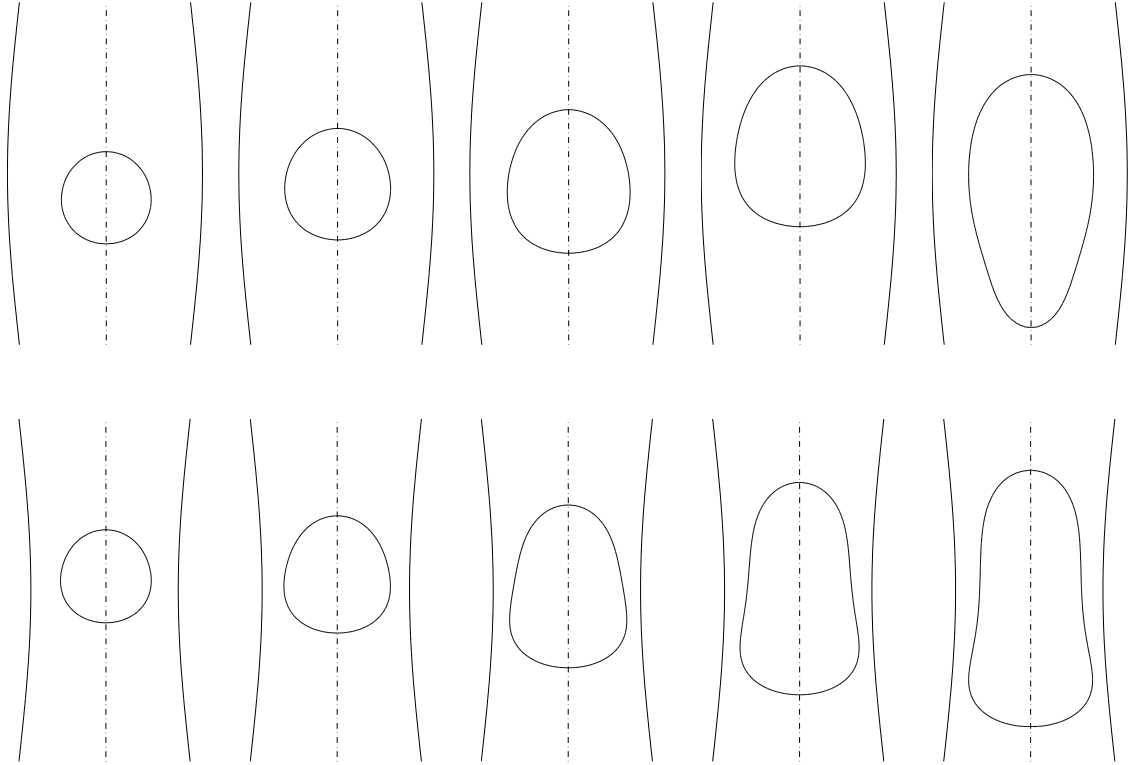
Figure 3.3: Snapshots of the drops at the expansion (upper plots) and at the throat (lower plots) of the constriction for the GW3 system for drop sizes (from left to right) $\kappa = 0.54$, 0.65, 0.78, 0.85 and 0.92, respectively. Grid: 32×1664, $\Delta t^* = 0.418$.

for D and L are partly attributed to the uncertainties in the experimental data and to the inconsistency between the Bond number reported by Hemmat and Borhan [5] and the Bond number computed from the material properties and the average tube radius as mentioned before.

Finally the computed average rise velocities are compared with the experimental data. The non-dimensional average rise velocity U_m is plotted against the non-dimensional drop size κ in Fig. 3.6a for GW3, GW5, DEGG10 and DEGG12 systems. The average rise velocity is defined as the average velocity of the drop centroid in the periodic motion. As can be seen in this figure, the numerical results are in a good agreement with the experimental data, i.e., the trend is well captured and the maximum error is less than 10% for all the cases. Note that there is no experimental data available for GW5 system but the numerical results for this system indicate a similar trend as the others. In addition, if the inconsistency
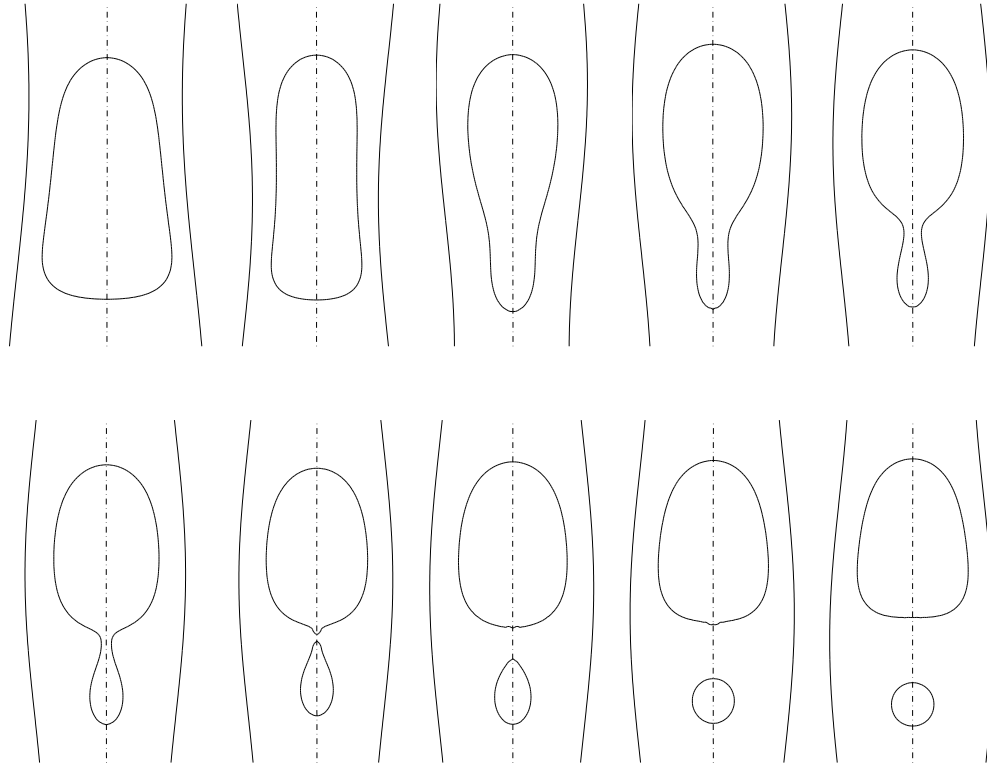
Figure 3.4: Evolution of a GW5 drop with $\kappa = 0.90$ in the constricted channel. The drop size is greater than the critical value so the drop breaks up. ($\alpha = 0.14$ and $\kappa_{cr} = 0.87$)

between the Bond numbers mentioned above is taken into account by modifying the average tube radius to match the Bond number reported in [5], the computed results compare much better with the experimental data as shown in Fig. 3.6b. In this case, the differences between the computed and experimental data reduce below a few percent at all the data points. In Fig. 3.6, the retardation effect of the constrictions is clearly seen and the non-dimensional velocity remains essentially constant for large drops, i.e., $\kappa > 0.90$ for all the cases.

(a)

(b)
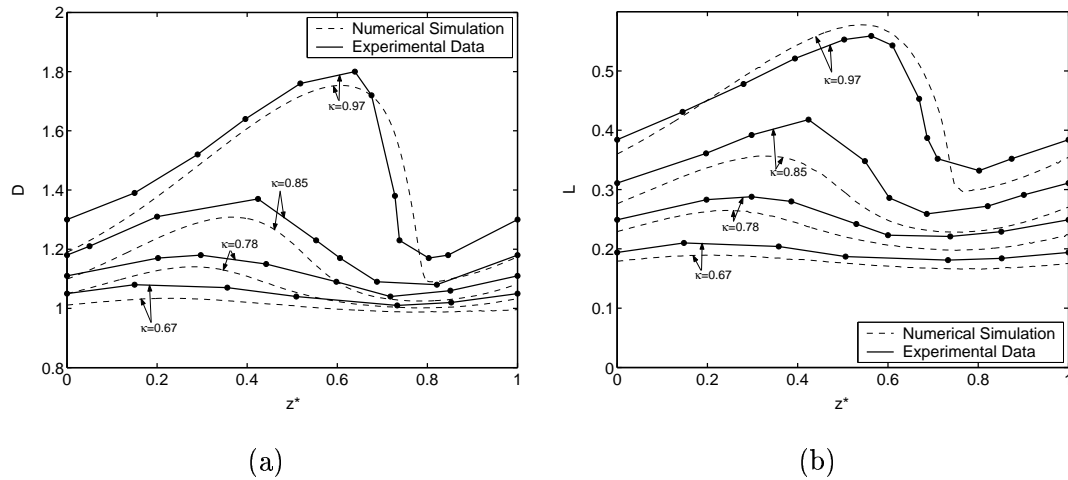
Figure 3.5: The variations of (a) the deformation parameter D and (b) the nondimensional axial drop length L with nondimensional axial position of the advancing meniscus within one period of corrugation for GW3 system. The dashed curves are the numerical results and the solid lines are the experimental data.

(a)

(b)
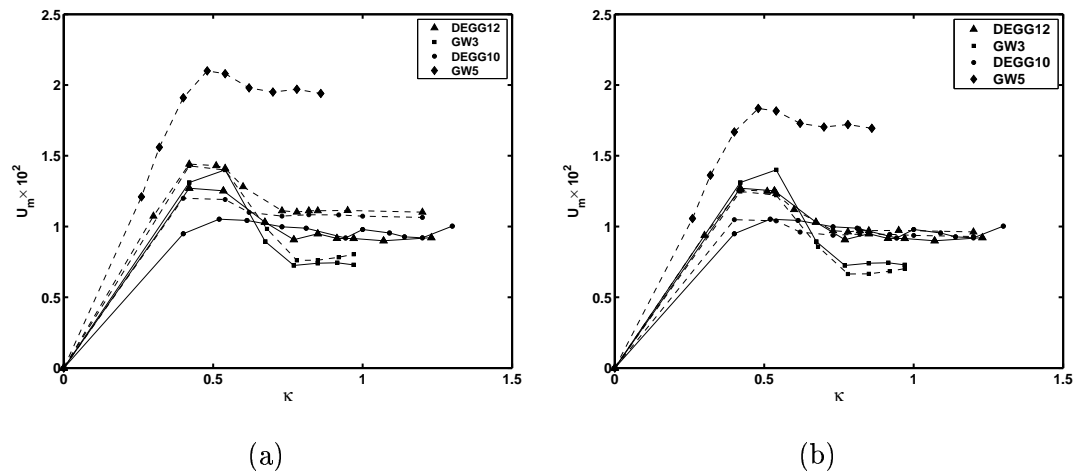
Figure 3.6: Dimensionless average rise velocity as a function of the nondimensional drop radius. The dashed curves are the numerical results and the solid lines are the experimental data. The numerical results are obtained with (a) the average tube radius of $R = 0.5$ cm and (b) the modified tube radius of $R = 0.535$ cm that yields the same Bond number given by Hemmat and Borhan [5].

3.2 Drop Breakup

After validating the computational results against the experimental data in the previous section, we now investigate the conditions for the onset of breakup. In all the results presented in this section, GW5 system is used as a base case. Note that $Bo = 12.91$ and $\alpha = 0.14$ correspond to the experimental conditions. The snapshots of drops are shown in Fig. 3.7 for different values of the non-dimensional drop size and Bond number in the capillary tube with the constriction parameter $\alpha = 0.28$. In the absence of a drop breakup, the snapshots are taken at the positions where the maximum necking is expected to occur. As can be seen in this figure, the critical drop size gets smaller as the Bond number increases. At low Bond numbers, i.e., $Bo < 15$, a drop breaks up into two or more drops of comparable size. As the Bond number increases, a drop breaks up into a large leading drop and many small trailing drops until the size of the leading drop gets smaller than the critical drop size when the initial drop size is equal or slightly larger than the critical value. This breakup mode resembles the tail streaming that typically occurs due to accumulation of surfactant at the back of the drop [14, 15]. On the other hand, if both the Bond number and drop size are large, the drops break up into two or more drops with comparable sizes.

It is interesting to observe that, when drop size is larger than the critical value, it breaks up into two or more drops such that the size of the leading drop remains nearly constant. This can be visually seen in Fig. 3.7 and is verified in Fig. 3.8 where the volume of the leading drop is plotted as a function of non-dimensional drop size. Note that the leading drop volume plotted in Fig. 3.4 is scaled by the volume of the drop the critical drop size denoted as V_{cr}. It is clearly seen in Fig. 3.8 that the leading drop volume remains nearly constant and multiple breakups occur when $\kappa > 0.8$ for this particular case. It is also seen in Fig. 3.7 that the trailing drop is small at critical drop size and increases rapidly as the size of the parent drop increases. To verify this observation, the ratio of the trailing drop volume to the leading drop volume is plotted in Fig. 3.9 as a function of non-dimensional drop size. As can be seen in this figure, trailing drop size is very small at the critical drop size and increases as the size of the parent drop increases. Note that, in the cases of multiple breakup, values are taken after the first breakup.

$$\kappa = 0.45 \quad \kappa = 0.55 \quad \kappa = 0.65 \quad \kappa = 0.75 \quad \kappa = 0.85$$

$Bo = 6.0$

$Bo = 12.91$

$Bo = 20.0$

$Bo = 40.0$

$Bo = 80.0$
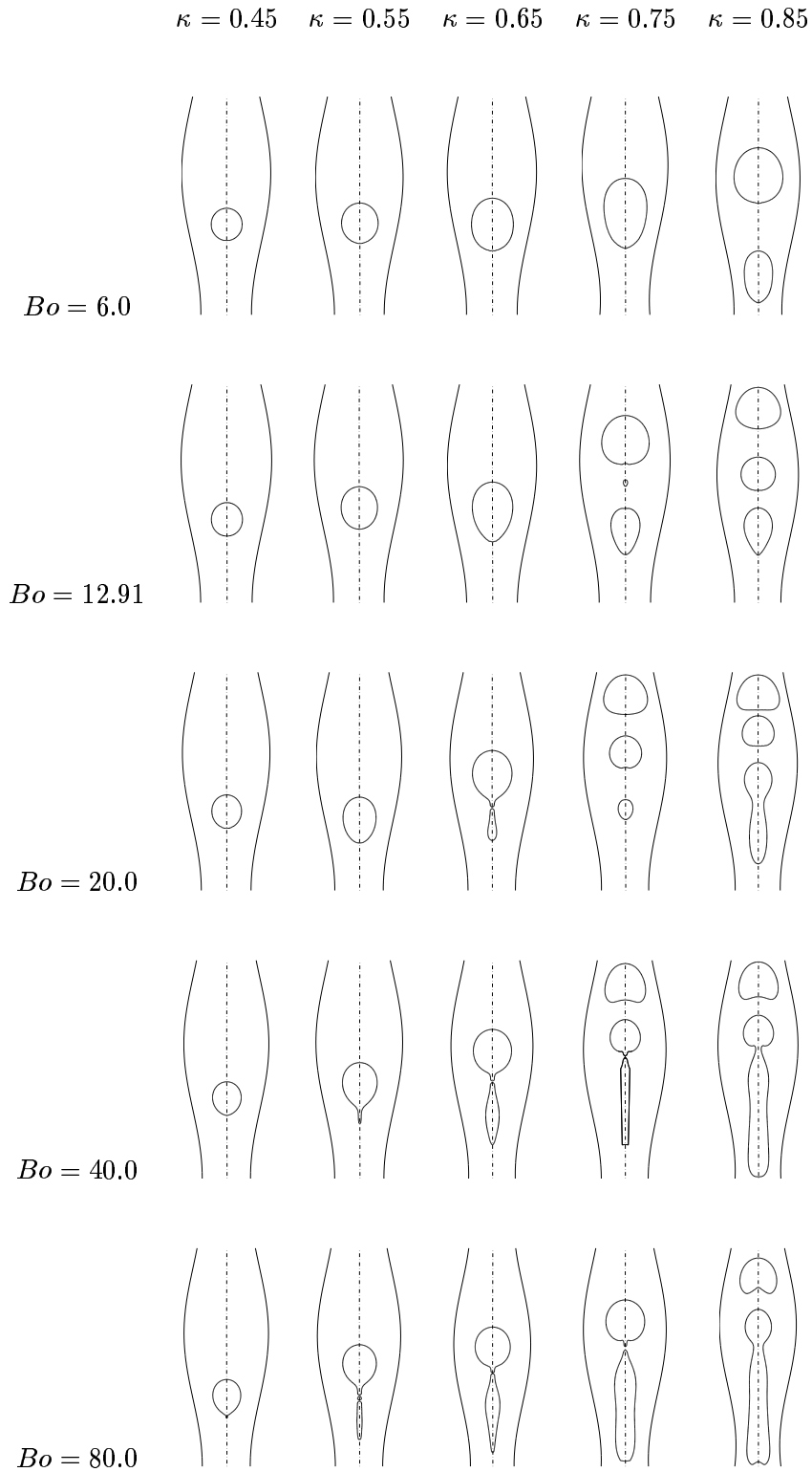
Figure 3.7: The effects of the drop size and Bond number on drop breakup. (The plots are not in the same scale and $\alpha = 0.28$.)
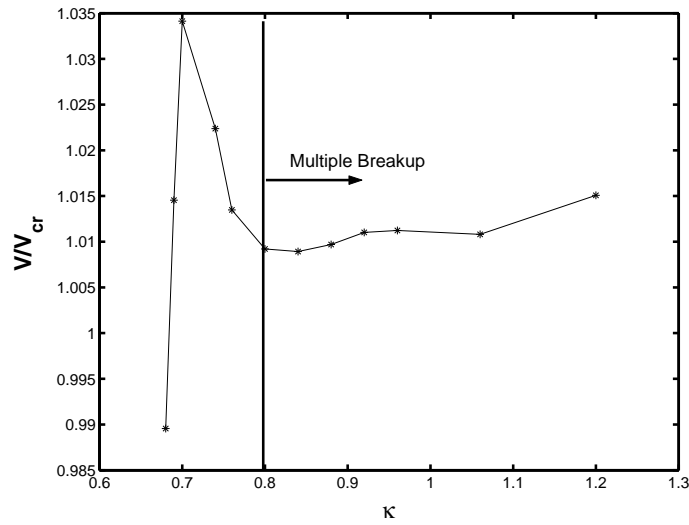
Figure 3.8: Nondimensional leading drop volume for GW5 system as a function of the nondimensional drop size ranging between $\kappa = \kappa_{cr} = 0.68$ and $\kappa = 1.20$. The drop volume is normalized by the value obtained at the critical drop size. ($\alpha = 0.28, Bo = 12.91$.)
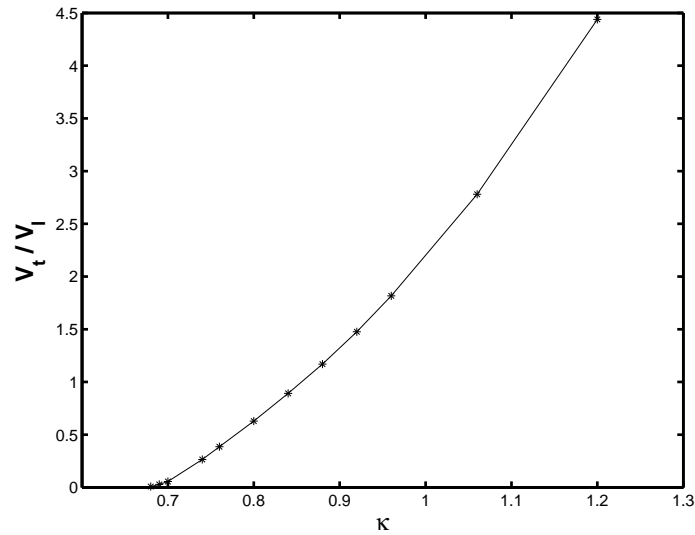
Figure 3.9: Ratio of the trailing drop volume to the leading drop volume for GW5 system as a function of the nondimensional drop size ranging between $\kappa = \kappa_{cr} = 0.68$ and $\kappa = 1.20$. The values are taken after the first breakup in multiple breakup cases. ($\alpha = 0.28, Bo = 12.91$)

Next the effects of the channel constriction on the evolution and breakup of the drops are shown in Fig. 3.10 for various Bond numbers. As can be seen in this figure, the critical drop size decreases as the level of constriction increases. At low Bond numbers, the drops may get stuck at the constrictions as seen in the case of $Bo = 6$ and $\alpha = 0.50$ in the figure. In this case, the buoyancy forces are not sufficient to force the drop through the constriction and are balanced by the surface tension forces leading eventually to a hydrostatic equilibrium. When the Bond number is made sufficiently large and the drop size is larger than the critical value, the drop breaks up into smaller drops in various modes as shown in the figure. Two representative examples are shown in Fig. 3.11 to better show the breakup mode at a high Bond number with a drop size equal or slightly larger than the critical value. As can be seen in this figure, this breakup mode resembles the tail streaming phenomena [14, 15]. A drop breaks up into two or more drops with comparable sizes if the drop size is sufficiently larger than the critical drop size. A multiple drop breakup process is shown in Fig. 3.12 as a representative example for this breakup mode.

As discussed above, drop breakup occurs in various modes depending on the Bond number, the non-dimensional drop size and the channel geometry. We now investigate the conditions for the breakup. First the critical non-dimensional drop size is plotted in Fig. 3.13 as a function of the constriction parameter α for various Bond numbers ranging between 6 and 80. As can be seen in this figure, in general, the critical nondimensional drop size κ_{cr} decreases with increasing values of α; and for a fixed α, κ_{cr} decreases as the Bond number increases. For a fixed Bond number, a breakup can occur only for a range of constriction parameter α and the range gets narrower as the Bond number decreases. For instance, in the experimental conditions, i.e., $Bo = 12.91$, a breakup occurs in the range $0.08 < \alpha < 0.5$. In the case of a straight channel, it is found that a breakup occurs only if $Bo \gtrsim 20.0$. For smaller values of Bo, a breakup may not occur even in the constricted channels independent of drop size. On the other hand, if the constriction is too severe, i.e., α is large, and the buoyancy forces are not sufficient to force the drop through the constrictions, i.e., Bo is small, a drop gets stuck at the throat. In this case, hydrostatic conditions are eventually established as buoyancy forces are balanced by the surface tension forces as discussed before.
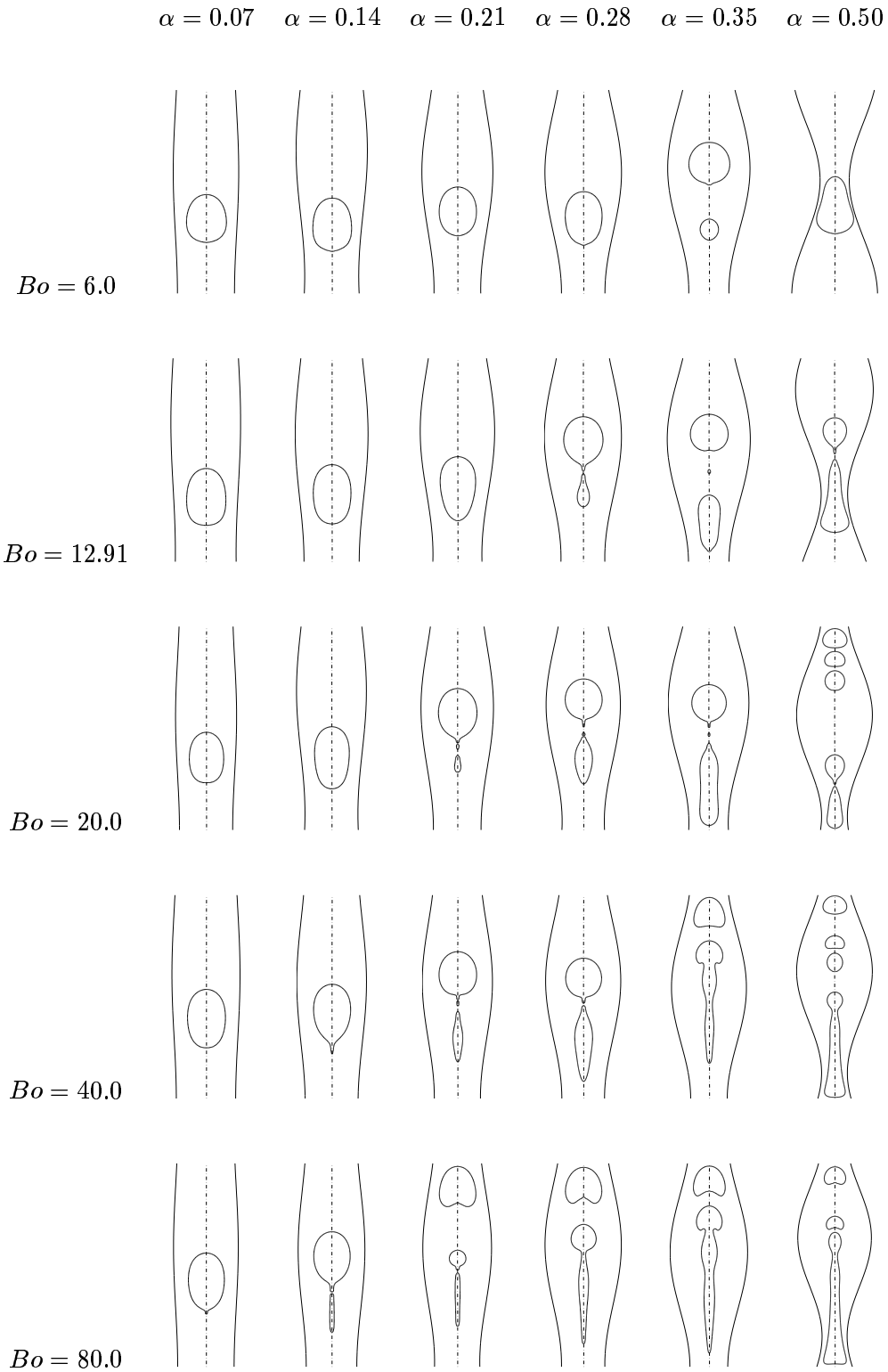
Figure 3.10: Effects of the channel constriction and the Bond number on drop breakup. (Plots are not in the same scale and $\kappa = 0.70$.)
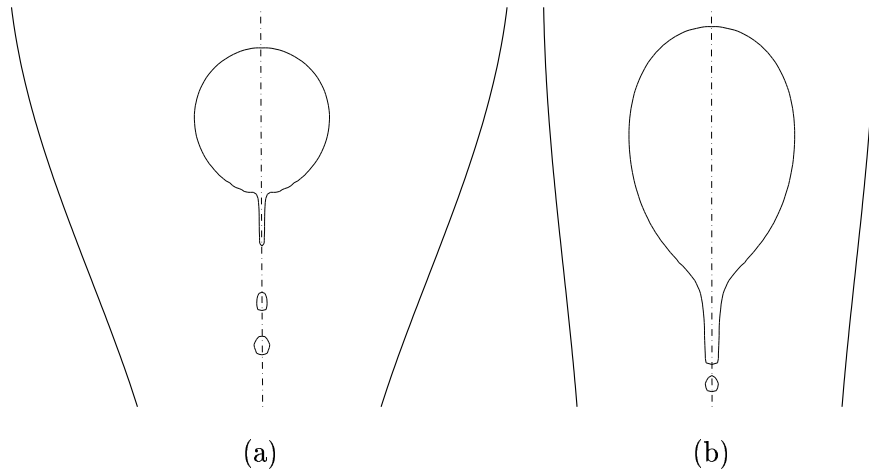
Figure 3.11: Typical drop breakups at high Bond number and the critical drop size. (a) Bo = 40.0 , $\alpha = 0.50$ and $\kappa = \kappa_{cr} = 0.41$; (b) Bo = 80.0 , $\alpha = 0.14$ and $\kappa = \kappa_{cr} = 0.65$.
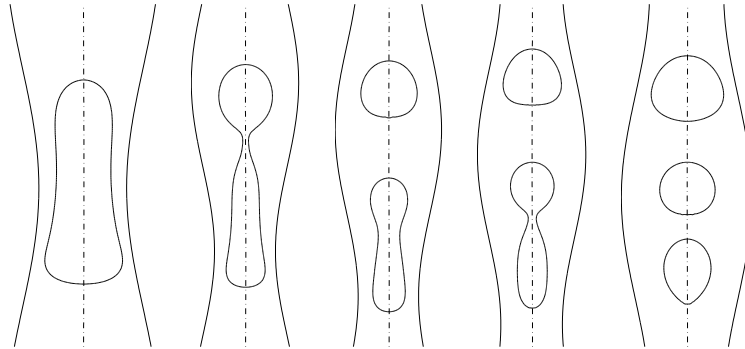
Figure 3.12: Snapshots showing the evolution of a large drop in a constricted channel. Time progresses from left to right and plots are not in the same scale. ($\kappa = 0.84$, $\kappa_{cr} = 0.68$, $\alpha = 0.28$ and $Bo = 12.91$.)

Figure 3.14 shows the ratio of the channel radius at the throat to the critical drop radius, $\Lambda_{cr} = R_{th}/R_{d_{cr}}$, as a function of the constriction parameter α for various values of the Bond number. As can be seen in this figure, Λ_{cr} generally increases with the Bond number. However it first increases, reaches a maximum and then decreases as α increases. This figure indicates that a breakup occurs the most effectively at moderate values of α.
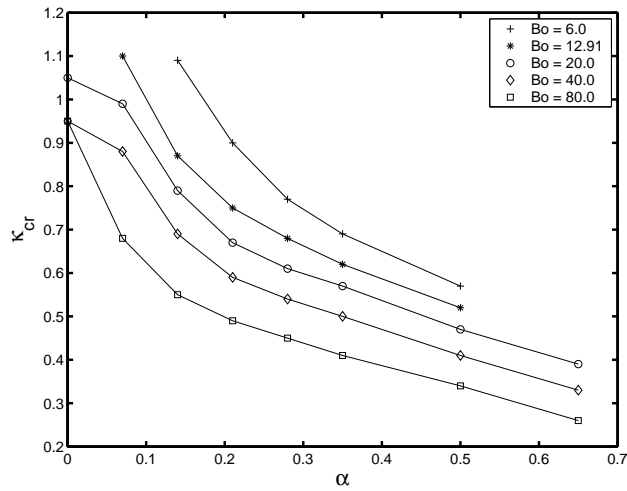
Figure 3.13: Dimensionless critical drop size (κ_{cr}) as a function of the channel constriction parameter (α) for different values of Bond number.
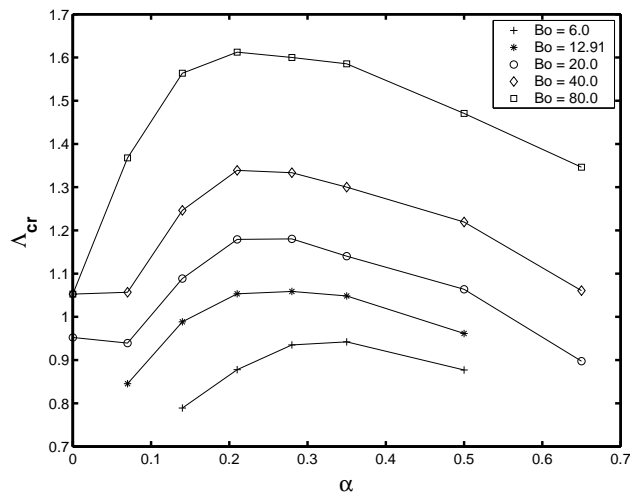
Figure 3.14: The ratio of the channel radius at the throat to the critical drop radius ($\Lambda_{cr} = R/R_{d_{cr}}$) as a function of the channel constriction parameter (α) for different values of Bond number.

Finally, critical capillary and buoyancy Reynolds numbers are defined as $Ca_{cr} = \mu U_{cr}/\sigma$ and $Re = (R^3 g \rho_o \Delta \rho)^{1/2}/\mu_o$, respectively, where U_{cr} is the average rise velocity of the drop at which a breakup occurs. The critical capillary number is plotted as a function of the buoyancy Reynolds number in Fig. 3.15 for various values of the Bond number and the constriction parameter α. It is clearly seen in this figure that the critical capillary number is essentially independent of the constrictions at small Bond numbers, i.e., $Bo < 6$ but it is increasingly influenced by the constrictions as the Bond number increases. It is also observed that the critical capillary number decreases as the constriction parameter increases.
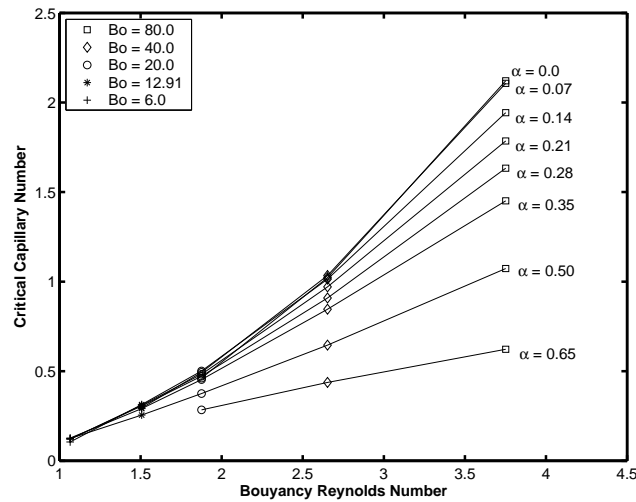
Figure 3.15: Critical capillary number versus buoyancy Reynolds number for different values of channel constriction parameter α.

Chapter 4

EFFECTS OF SURFACTANT ON THE DYNAMICS OF VISCOUS DROPS

In this chapter, the effect of surfactants on the dynamics of buoyancy-driven viscous drops is investigated. As discussed in the Introduction in Chapter 1, surfactants are either present as impurities or added to the system deliberately since they decrease the interfacial tension considerably. This decrease in the surface tension leads to interfacial tension gradients along the fluid-fluid interface. These gradients result in tangential (Marangoni) stresses which affect the motion of the interface. Hence, understanding the effects of surfactants properly is essential.

Concentration of surfactant, Γ, is defined as

$$\Gamma = \frac{M_s}{A}, \tag{4.1}$$

where M_s is the total mass of surfactant and A is the surface area. Because of the dimensional limitations, Γ can not exceed a maximum surface limit, Γ_{inf}. When the surfactant concentration is well below the saturation limit, i.e., $\Gamma << \Gamma_{inf}$, a linear relationship may be assumed between the surface tension and the surface concentration according to Gibbs' law [29],

$$\sigma_s - \sigma = \Gamma \mathcal{R} \mathcal{T}, \tag{4.2}$$

where $\mathcal{R}$ is the ideal gas constant, T is the absolute temperature, σ_s is the surface tension of clean interface. Rearranging the linear surface tension equation of state yields,

$$\sigma = \sigma_s (1 - \beta \frac{\Gamma}{\Gamma_{inf}}), \tag{4.3}$$

where $\beta = \Gamma_{inf} RT/\sigma_s$ is a dimensionless coefficient related to the surface elasticity by $E = \sigma_s \beta/\Gamma_{inf}$ and it varies between zero (no surfactant effect) and unity. The linear surface equation of state is used and β is taken as 0.65 in the computations presented in this chapter.

In the next section, the governing equations for the disperse multiphase flow with surfactants are described and they are nondimensionalized. Then, the numerical algorithm is presented. The accuracy of the numerical algorithm is demonstrated in Section 4.2 using simple test cases for which analytical solutions are available. Finally, in Section 4.3, the results are presented and discussed.

4.1 Mathematical Formulation

The surfactant concentration Γ evolves by [31],

$$\frac{\partial \Gamma}{\partial t} + \nabla_s \cdot (\Gamma \mathbf{U}_s) = D_s \nabla_s^2 \Gamma + \dot{S}_\Gamma, \tag{4.4}$$

where the gradient operator along the interface is defined as,

$$\nabla_s = \nabla - n(n \cdot \nabla), \tag{4.5}$$

where n is the outward normal vector and $\mathbf{U}_s$ is the tangential velocity on the interface. In Eq. (4.4), D_s represents the diffusion coefficient along the interface and $\dot{S}_\Gamma$ is the source term given by,

$$\dot{S}_\Gamma = \beta_s C_s (\Gamma_{\text{inf}} - \Gamma) - \alpha_s \Gamma, \tag{4.6}$$

where α_s and β_s are desorption and adsorption coefficients, respectively, Γ_{inf} is the maximum possible surfactant concentration and C_s is the concentration of surfactant in fluid immediately adjacent to the interface. The bulk surfactant concentration C is governed by,

$$\frac{\partial C}{\partial t} + \nabla \cdot (C\mathbf{U}) = D_c \nabla^2 C, \tag{4.7}$$

where D_c is the molecular diffusion coefficient. The source term in Eq. (4.4) is related to the bulk concentration as [33],

$$\dot{S}_\Gamma = n.\nabla C|_{interface}. \tag{4.8}$$

In the present work, the bulk concentration is assumed to remain constant, i.e., $C_s = 1.0$. Therefore Eq. (4.6) reduces to,

$$\dot{S}_\Gamma = \beta_s (\Gamma_{\text{inf}} - \Gamma) - \alpha_s \Gamma. \tag{4.9}$$

At equilibrium Eq. (4.4) becomes,

$$cov = \frac{\Gamma_{eq}}{\Gamma_{inf}} = \frac{k}{1+k}, \tag{4.10}$$

where cov is the surfactant coverage, Γ_{eq} is the equilibrium surfactant concentration and k is the adsorption number defined as the ratio of characteristic adsorption to desorption rates,

$$k = \frac{\beta_s}{\alpha_s}. \tag{4.11}$$

First, the surfactant evolution equation is nondimensionalized using the length scale $L = R$, velocity scale $V = \frac{\Delta \rho g R^2}{\mu}$ and time scale $T = \frac{\mu}{\Delta \rho g R}$, where R is the radius of the channel, μ is the velocity of the bulk fluid, $\Delta \rho$ is the density difference between the drop and bulk fluids and g is the gravitational acceleration. The resulting equation is given by

$$\frac{\partial \Gamma^*}{\partial t^*} + \nabla_s^* \cdot (\Gamma^* \mathbf{U}^*) = \frac{1}{Pe} \nabla_s^{*2} \Gamma^* + Bi(1+k)(1-\Gamma^*), \tag{4.12}$$

where Pe and Bi are the Peclet and Biot numbers, respectively, defined as,

$$Pe = \frac{\Delta \rho g R^3}{\mu D_s}, \quad Bi = \frac{\mu \alpha}{\Delta \rho g R}. \tag{4.13}$$

In the present study, the surfactant concentration equation is solved in the dimensional form, i.e., Eq. (4.4). From Eq. (4.4) and (4.5), we obtain,

$$\frac{\partial \Gamma}{\partial t} + \nabla \cdot (\Gamma \mathbf{U}_s) - \Gamma n \cdot \nabla \mathbf{U}_s \cdot n = D_s \nabla_s^2 \Gamma + \dot{S}_\Gamma. \tag{4.14}$$

On the other hand, an area element on the interface evolves by the following equation [32],

$$\frac{DA}{Dt} = \frac{\partial A}{\partial t} + \mathbf{U} \cdot \nabla A = -A(n \cdot \nabla U \cdot n). \tag{4.15}$$

Combining Eq. (4.14) and (4.15) and rearranging the terms yields,

$$\frac{d\Gamma A}{dt} = AD_s \nabla_s^2 \Gamma + A\dot{S}_\Gamma. \tag{4.16}$$

In an axisymmetric problem that would be of interest Eq. (4.16) can be written as,

$$\frac{d\Gamma A}{dt} = A[D_s \frac{1}{r} \frac{\partial}{\partial s} (r \frac{\partial \Gamma}{\partial s}) + \dot{S}_\Gamma], \tag{4.17}$$

where s is the arclength along the interface and r is the radial coordinate in cylindrical coordinates. Eq. (4.17) can be expressed as

$$\frac{d\Gamma A}{dt} = Af(\Gamma, t), \tag{4.18}$$

where function f is given by,

$$f(\Gamma, t) = D_s \frac{1}{r} \frac{\partial}{\partial s} (r \frac{\partial \Gamma}{\partial s}) + \dot{S}_\Gamma. \tag{4.19}$$

The right hand side of Eq. (4.17) is discretized using central differences as,

$$[Af]_k \cong \frac{A_k}{r_k} D_s [\frac{r_{k+\frac{1}{2}} \frac{\Gamma_{k+1} - \Gamma_k}{s_{k+1} - s_k} - r_{k-\frac{1}{2}} \frac{\Gamma_k - \Gamma_{k-1}}{s_k - s_{k-1}}}{s_{k+\frac{1}{2}} - s_{k-\frac{1}{2}}}] + A_k \dot{S}_{\Gamma_k}, \tag{4.20}$$

where k denotes the kth front element. Defining $\Delta s_k = s_{k+\frac{1}{2}} - s_{k-\frac{1}{2}}$ and using $A_k \cong \frac{1}{2}(r_{k+\frac{1}{2}} + r_{k-\frac{1}{2}})\Delta s_k \cong r_k \Delta s_k$, we obtain,

$$[Af]_k \cong D_s \frac{r_{k+\frac{1}{2}} \frac{\Gamma_{k+1} - \Gamma_k}{\Delta s_{k+\frac{1}{2}}} - r_{k-\frac{1}{2}} \frac{\Gamma_k - \Gamma_{k-1}}{\Delta s_{k-\frac{1}{2}}}}{r_k} (\Gamma_{k+\frac{1}{2}} - \Gamma_{k-\frac{1}{2}}) + A_k \dot{S}_{\Gamma_k}. \tag{4.21}$$

The time-integration is performed in two steps. In advancing solutions from physical time level n ($t_n = n \cdot \Delta t$) to level $n + 1$, the surfactant concentration Γ on the interface at the new time level $n + 1$ are first predicted as,

$$\widetilde{\Gamma}^{n+1} \widetilde{A}^{n+1} = \Gamma^n A^n + \Delta t A^n f(\Gamma^n, t_n). \tag{4.22}$$

Then the surface tension coefficient σ is evaluated from the equation of state, i.e., Eq. (4.3) and the interface is moved according to Eq. (2.15) and then $\widetilde{A}^{n+1}$ is evaluated based on the predicted interface location. Finally, the surfactant concentration at the new time level $n + 1$ is corrected as,

$$\Gamma^{n+1} A^{n+1} = \Gamma^n A^n + \frac{\Delta t}{2}[A^n f^n + \widetilde{A}^{n+1} \widetilde{f}^{n+1}]. \tag{4.23}$$

Taking $A^n f^n$ from Eq. (4.22) and substituting it into Eq. (4.23) yields,

$$\Gamma^{n+1} A^{n+1} = \Gamma^n A^n + \frac{\Delta t}{2}[\frac{\widetilde{\Gamma}^{n+1} \widetilde{A}^{n+1} - \Gamma^n A^n}{\Delta t} + \widetilde{A}^{n+1} \widetilde{f}^{n+1}]. \tag{4.24}$$

Introducing $\phi = \Gamma A$, the surfactant concentration at the new time level $n + 1$ is computed as,

$$\Gamma^{n+1} = \frac{1}{2}[\frac{\phi^n + \widetilde{\phi}^{n+1}}{A^{n+1}}] + \frac{\Delta t}{A^{n+1}}[\widetilde{A}^{n+1} f(\widetilde{\Gamma}^{n+1}, t_{n+1})]. \tag{4.25}$$

4.2 Validation of the Numerical Algorithm

In order to validate the numerical solution algorithm, each term in Eq. (4.17) is tested individually and results are compared with the analytical solutions for simple test cases.

4.2.1 Source term

First the interface is kept stationary and the diffusion coefficient D_s is set to zero. In this case, Eq. (4.17) reduces to,

$$\frac{d\Gamma}{dt} = \beta_s \Gamma_{\text{inf}} - (\alpha_s + \beta_s)\Gamma, \tag{4.26}$$

which can be integrated in time to obtain the analytical solution as,

$$\Gamma = \frac{\beta_s \Gamma_{\text{inf}}}{\alpha_s + \beta_s}[1 - e^{-(\alpha_s + \beta_s)t}]. \tag{4.27}$$

A stationary drop of radius R is initialized and the surfactant concentration is initially set to zero. Thus, the surfactant concentration Γ increases just because of the source term. In Fig. 4.1, a comparison of the numerical and analytical solutions is shown for different Biot numbers. Increasing the Biot number leads to a discrepancy between the numerical and analytical solutions mainly due to large time-stepping error. As shown in Fig. 4.2, when the time-step is reduced, the numerical results match much better with the analytical solution even for Bi = 1.0. Note that the results are presented in terms of nondimensional quantities in Figs. 4.1 and 4.2.
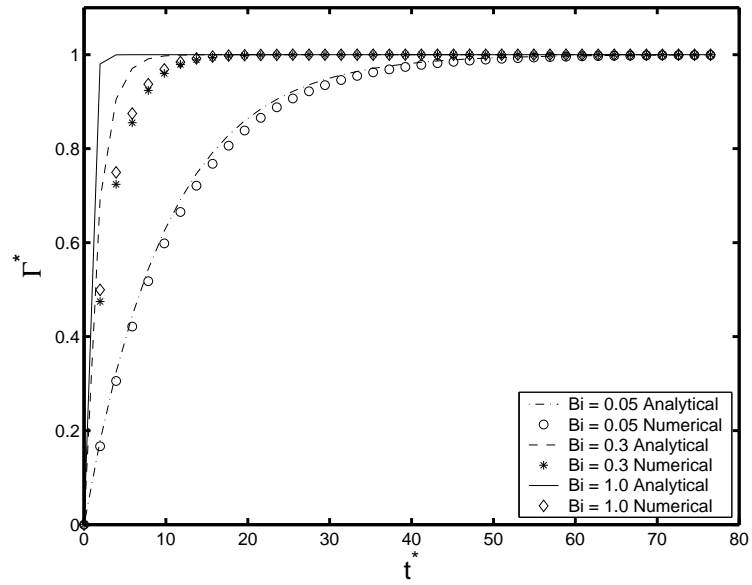
Figure 4.1: Evolution of surfactant concentration for various Biot numbers when diffusion is switched off. ($\Delta t^* = 1.9620$)
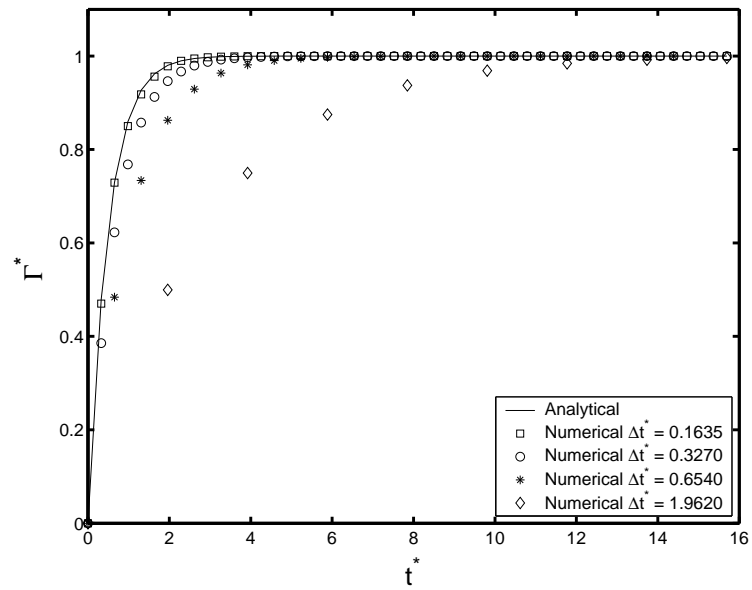

Figure 4.2: Evolution of surfactant concentration for various time steps when diffusion is switched off. ($Bi = 1.0$)

4.2.2   Diffusion terms

In order to test the diffusive terms, a cylindrical interface is kept stationary and the source term $\dot{S}_\Gamma$ is switched off. In this case, Eq. (4.17) reduces to,

$$\frac{\partial \Gamma}{\partial t} = \frac{D_s}{r}\frac{\partial}{\partial s}(r\frac{\partial \Gamma}{\partial s}). \tag{4.28}$$

As shown in Fig. 4.3, a sinusoidal initial surfactant concentration is distributed over a cylinder. In this case, Eq. (4.17) becomes,

$$\frac{\partial \Gamma}{\partial t} = D_s \frac{\partial^2 \Gamma}{\partial z^2}, \tag{4.29}$$

which can be solved analytically using a separation of variables method and the solution is given by,

$$\Gamma(z,t) = 1 + [\cos \frac{\pi z}{H}] e^{-(D_s \frac{\pi^2}{H^2} t)}. \tag{4.30}$$

The numerical results are compared with the analytical solution in Fig. 4.4. As can be seen in this figure, the numerical results match very well with the analytical solution showing the accurate discretization of the diffusive terms.

4.2.3   Convection terms

In this case an expanding sphere is considered and both the diffusion and source terms are switched off in order to test the numerical approximation to the convective terms. For this case, Eq (4.17) simply becomes,

$$\frac{d\Gamma A}{dt} = 0. \tag{4.31}$$

The surfactant concentration is initially distributed homogeneously on the spherical interface and let the interface expand continuously in the normal direction as shown in Fig. 4.5. As the interface expands, the surfactant concentration is given by,

$$\Gamma(t) = \frac{A_o}{A(t)}\Gamma_o, \tag{4.32}$$

where A_o and Γ_o are the initial interfacial surface area and the initial surfactant concentration, respectively, while $A(t)$ and $\Gamma(t)$ are the values at time t. The numerical and analytical solutions for the variation of surfactant concentration in time are plotted in Fig. 4.6. As can be seen in this figure, the numerical results are in a very good agreement with the analytical solution.

Figure 4.3: Schematic representation of the initial configuration of the computational domain used to test discretization of diffusion terms.

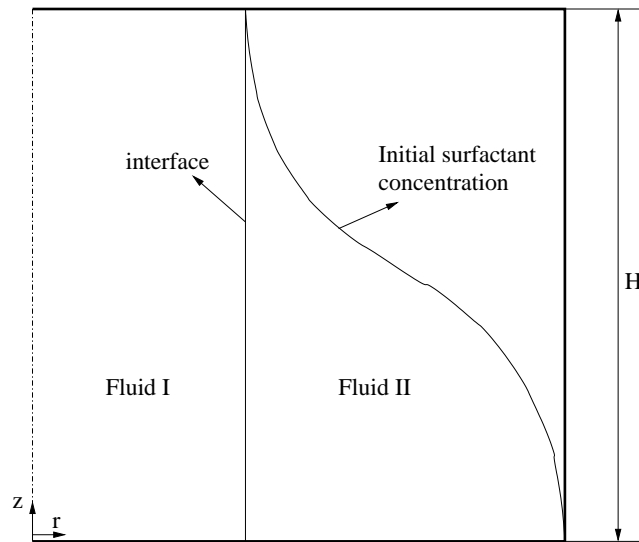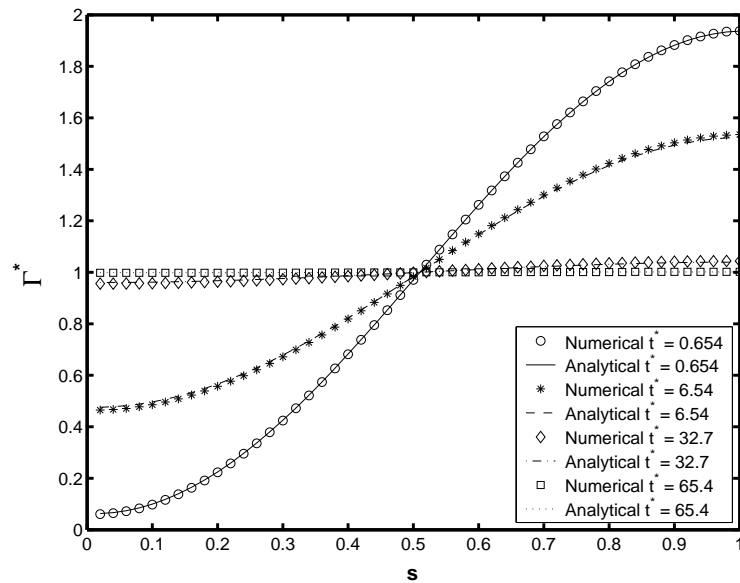Figure 4.4: Evolution of surfactant concentration when source term is switched off. ($Pe = 100.0$, $\Delta t^* = 0.6540$)
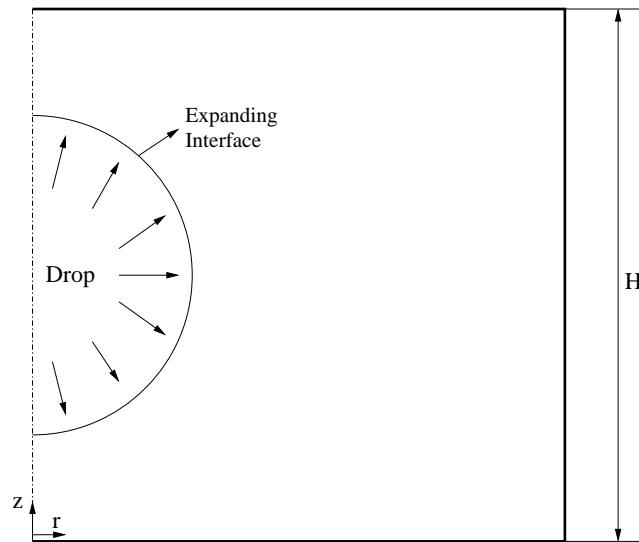
Figure 4.5: Schematic representation of the configuration of the computational domain used to test discretization of convection terms.
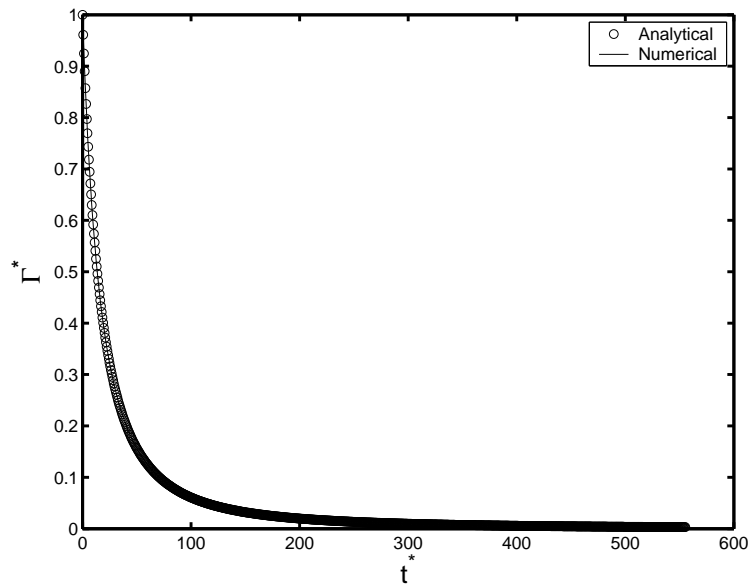

Figure 4.6: Evolution of surfactant concentration in time for a continuously expanding spherical interface.

4.3   Drops Moving in Capillaries

After validating the numerical solution algorithm for simple test cases in the previous section, the method is now applied to study the effects of surfactant on the motion and breakup of drops moving in straight and constricted capillaries. The results are qualitatively compared with the available experimental data.

The method is first applied to the cases in straight channels experimentally studied by Almatroushi and Borhan [17] and then the effects of surfactant coverage and Bond number are investigated in constricted channels for GW5 system of the previous chapter. The experimental setup used by Almatroushi and Borhan [17] is consisted of a vertical tube of inside diameter 0.796cm and length 120cm. Aqueous glycerol solutions (96.2 wt%) is used as the suspending fluid. UCON LB-165 fluid were used as drop fluid. The suspending fluid has a density of 1247 kg/m^3 and a viscosity of 443 mPa.s and the drop fluid has a density of 976 kg/m^3 and a viscosity of 100 mPa.s. They used various amounts of 99%+ pure sodium dodecyl sulfate (SDS) to dissolve in the suspending fluid in order to prepare surfactant solutions of various concentrations. The interfacial tension of the surfactant-free interface is 0.008 N/m. The computations are performed using a grid with 32x832 grid cells. A drop with diameter d and radius R_d is instantaneously placed in the ambient fluid that fully fills the cylindrical tube and is initially in the hydrostatic conditions. The drop is initially spherical if its initial radius is smaller than the radius of the capillary tube and is ellipsoidal otherwise. The drop begins to rise due to the density difference of the drop and suspending fluid. First a qualitative analysis of the steady shapes of the drop is presented in Fig. 4.7 for the nondimensional drop sizes of $\kappa = 0.40, 0.50, 0.60, 0.70, 0.80$ and 1.00. As a drop rises in the tube, it eventually reaches steady-state, obtaining a steady shape and a constant velocity. The steady shapes of the drops in Fig. 4.7 qualitatively compare very well with the experimental observations of Almatroushi and Borhan [17]. In Fig. 4.8, the computed average rise velocities of drops are presented. As can be seen in this figure, the numerical results match well with the experimental results for the surfactant-free case and the trend with increasing values of surfactant coverage is similar to the experimental observations. In the experiments, Almatroushi and Borhan [17] increased the surfactant concentration gradually and observed that the rise velocity does not change significantly for small drops, whereas it increases by %50 with high surfactant concentrations for large drops. This is

because an increase in the surfactant concentration leads to a smaller radial dimension or, equivalently, a thicker liquid film between the drop and the tube wall. This increase in the distance between large drops and the tube wall causes a significant improvement in their mobility because of the viscous nature of the drop phase.

$\kappa = 0.40$ $\kappa = 0.50$ $\kappa = 0.60$ $\kappa = 0.70$ $\kappa = 0.80$ $\kappa = 1.00$
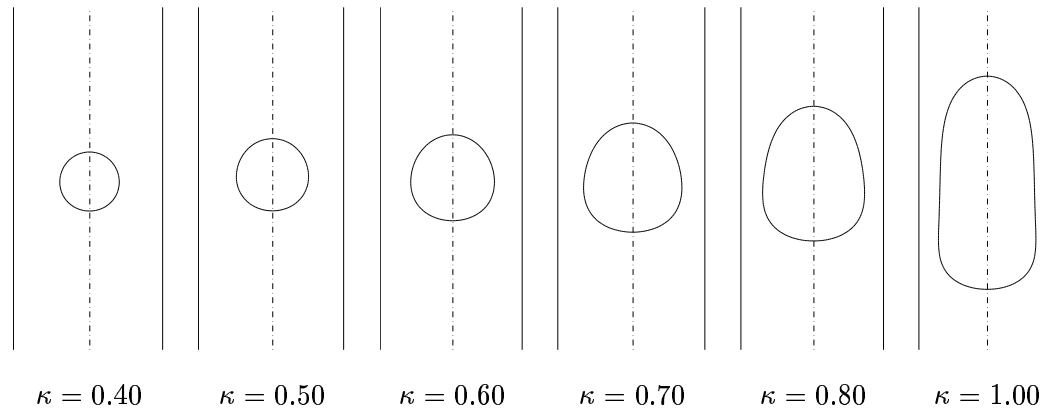
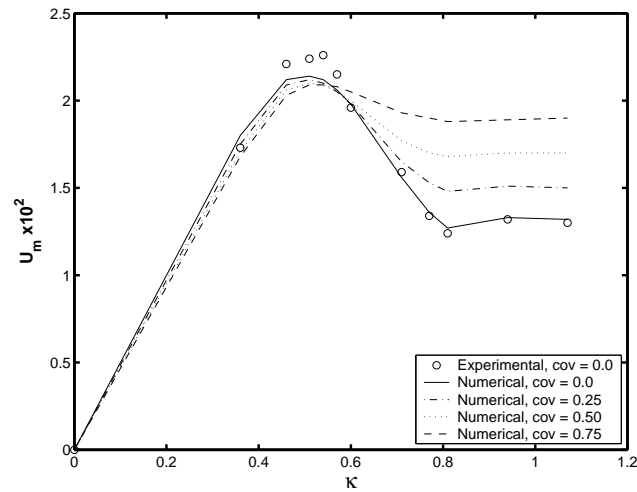Figure 4.7: Snapshots of drops for $cov = 0.50$

Figure 4.8: Effect of surfactant coverage on the rise velocity of viscous drops

To better see the effects of surfactant coverage on breakup, coverage value is gradually increased for nondimensional drop sizes of $\kappa = 0.60, 0.70, 0.80$ and 0.90 in Fig. 4.9. The computations are performed for Bo $= 12.91$ and $\alpha = 0.14$ for which the critical nondimensional drop size is $\kappa_{cr} = 0.87$. All snapshots are taken after the drops passed the first constriction. No breakup is observed before the first constriction in any case. The general trend is that increasing surfactant coverage enhances breakup and induces tail-streaming as was also observed by Eggleton et al. [25]. The critical nondimensional drop size κ_{cr} decreases down to 0.80 for $cov = 0.50$ and to 0.70 for $cov = 0.95$. Also, the mode of breakup turns to be more like tail-streaming for increasing values of coverage. For example, for $\kappa = 0.90$, the regular mode of breakup is observed for the surfactant-free case, whereas the trailing drop stretches in the vertical direction with increasing values of coverage and tail-streaming is observed for $cov = 0.95$.

The surfactant concentration distribution for a drop with $\kappa = 0.80$ is presented in Fig. 4.10. The distributions are taken just before breakup for $cov = 0.50, 0.75$ and 0.90. The distribution for $cov = 0.25$ where no breakup occurs is taken at the position where maximum necking is expected to occur. In all the surfactant coverage values, Γ_{eq} is 1.0 and s is the arclength measured in clockwise direction. It is clearly seen that surfactant is swept away from the leading part of the drop to the trailing part as was also observed by Stone et al. [23] and Eggleton et al. [25]. For $cov = 0.25$ where no tail-streaming occurs, maximum surfactant concentration is obtained at the very tip of the drop, whereas the maximum concentration is reached at the locations where the tail-streaming starts for $cov = 0.50, 0.75$ and 0.95.
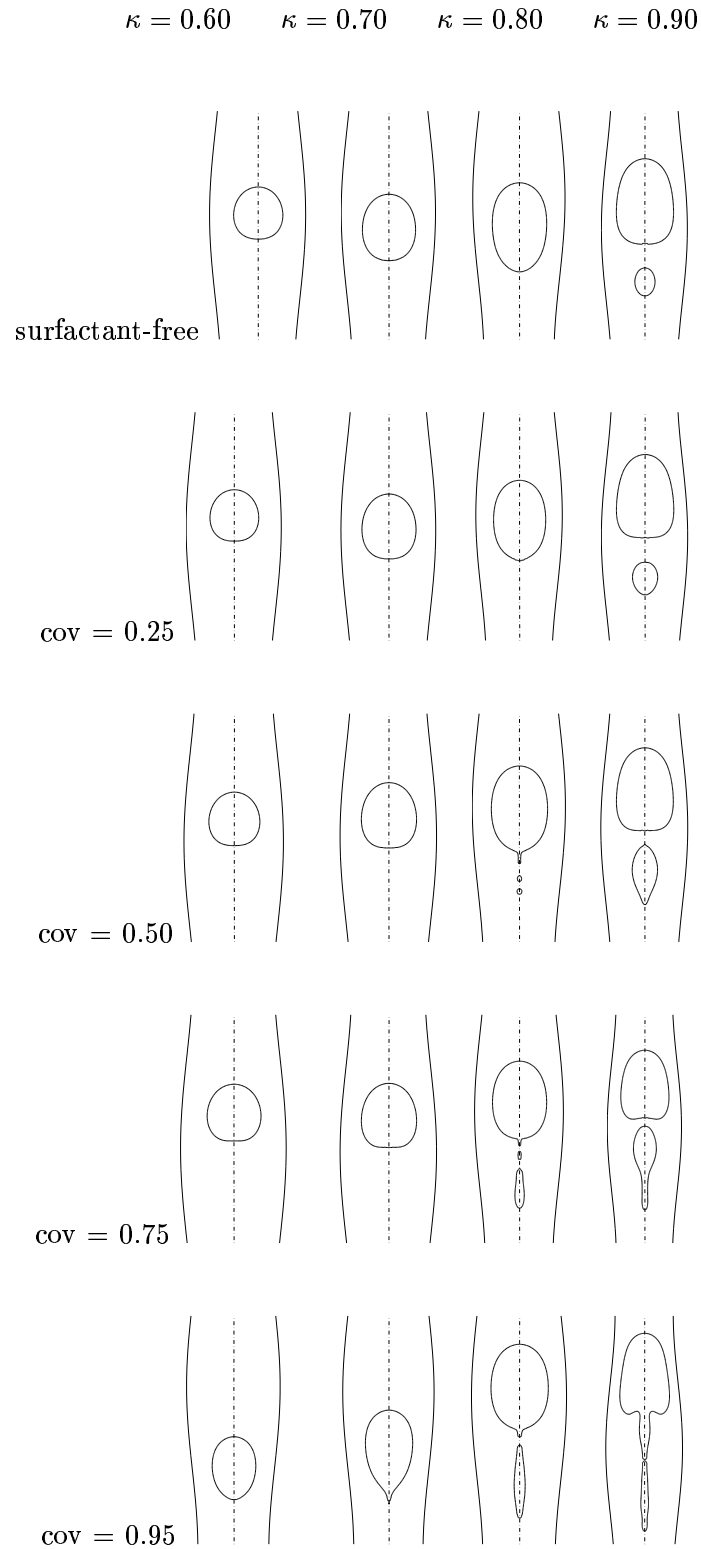
Figure 4.9: Snapshots of drops for various surfactant coverage values. Note that κ_{cr} is 0.87 for the surfactant-free case. ($Bo = 12.91$ and $\alpha = 0.14$)
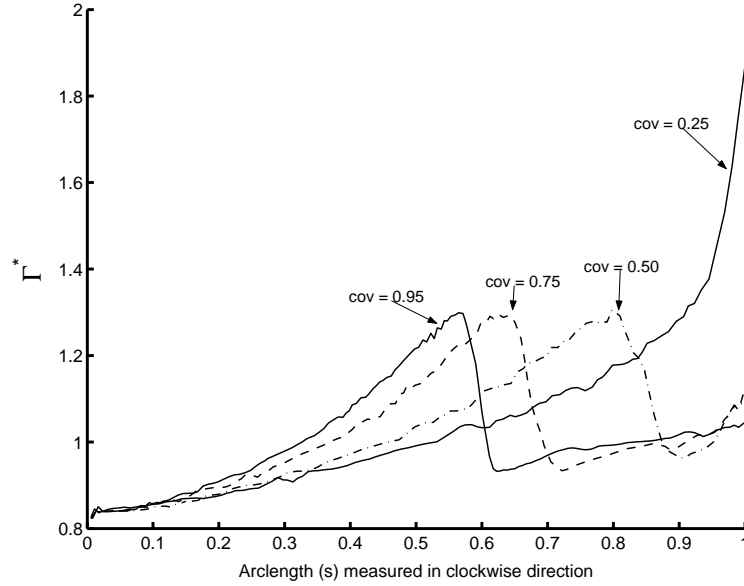
Figure 4.10: Surfactant concentration profiles for $\kappa = 0.80$ drops for various surfactant coverage values just before breakup occurs

Snapshots of $\kappa = 0.70$ drops are presented in Fig. 4.11 for various surfactant coverage values and Bond numbers. The general trend is again the enhancement of breakup and tail-streaming with increasing values of surfactant coverage and Bond number. However, for high Bond numbers, such as Bo $= 80.0$, a re-entrant cavity is formed at the trailing end of the drop before it passes the first constriction. It is observed that the re-entrant cavity is larger for higher coverage values. Just after the time-step of these snapshots shown in Fig. 4.11, the tip of the re-entrant cavity tends to break up into a small droplet inside the main drop which can not be simulated with the current implementation of the method. This re-entrant cavity resembles the one observed by Tsai and Miksis [26]. They showed that increasing β, i.e., increasing the diverse effect of surfactant on surface tension, enhances the formation of re-entrant cavity. In Fig. 4.12, snapshots of a drop with the nondimensional drop size $\kappa = 0.70$ for $cov = 0.95$ and $Bo = 80.0$ are presented for various values of β. The enhancing effect of surfactant on the formation of re-entrant cavity is clearly seen in this figure. There occurs almost no re-entrant cavity for $\beta = 0.0$, whereas the degree of it increases with β and the tip of the re-entrant cavity reaches the leading tip of the drop for $\beta = 0.95$.

$Bo = 12.91$ $Bo = 20.0$ $Bo = 40.0$ $Bo = 80.0$

surfactant-free

cov = 0.25

cov = 0.50

cov = 0.75

cov = 0.95
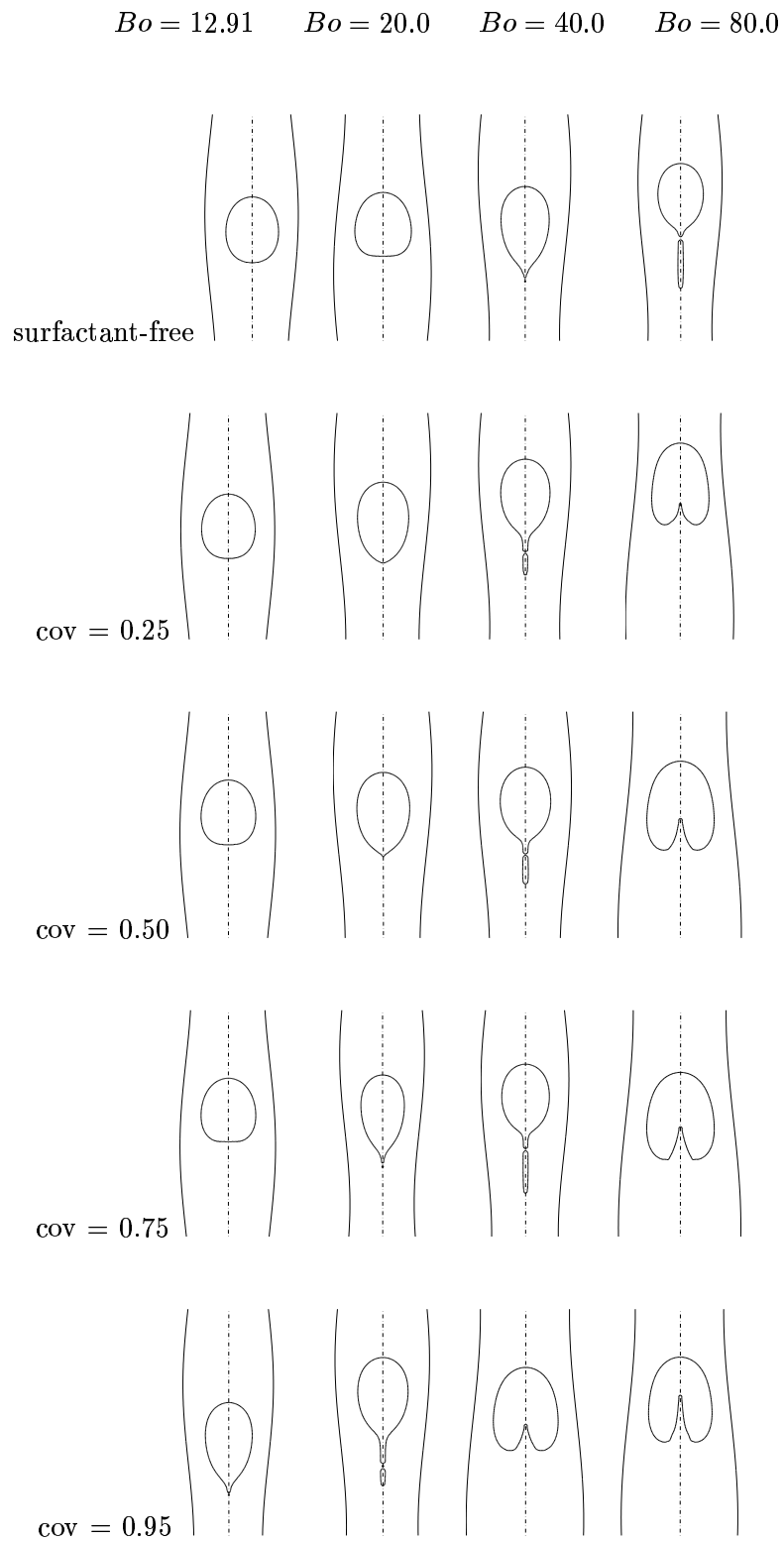
Figure 4.11: Snapshots of a $\kappa = 0.70$ drop for various surfactant coverage values and Bond numbers.($\alpha = 0.14$)

$\beta = 0.0$ $\beta = 0.10$ $\beta = 0.20$ $\beta = 0.35$ $\beta = 0.50$ $\beta = 0.65$ $\beta = 0.80$ $\beta = 0.95$
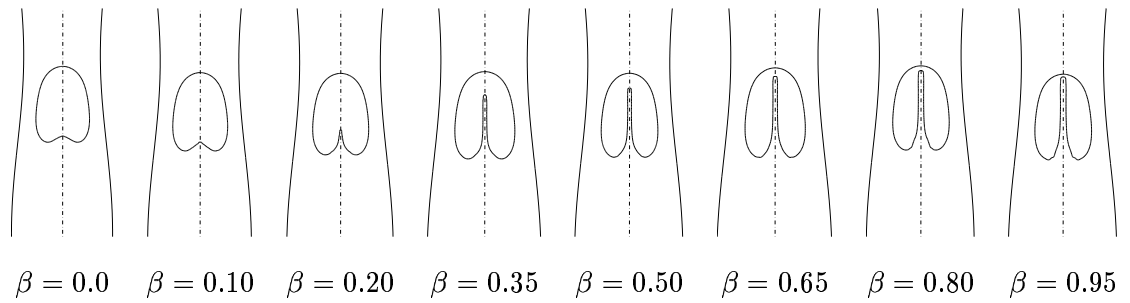
Figure 4.12: Snapshots of drops showing re-entrant cavity for $cov = 0.95$ and $Bo = 80.0$. ($t^* = 13.08$ for all the snapshots)

Chapter 5

CONCLUSIONS

Buoyancy-driven motion and breakup of viscous drops in constricted capillaries including the effects of soluble surfactants are studied computationally using a finite-volume/front-tracking method. Computational results are first compared with the available experimental data and are found to be in a good agreement. The breakup modes of viscous drops are examined for a wide range of non-dimensional drop sizes, channel geometries, Bond numbers and coverage values. It is found that a drop breakup occurs when the size of drop is larger than a critical value in various modes depending on the relative drop size, channel constriction, Bond number and initial coverage value for the surfactant concentration. When the Bond number is large, a drop breaks up into a large leading drop and many smaller trailing drops for the drop sizes equal or slightly larger than the critical value. This breakup mode resembles the tail streaming phenomena. As drop size is further increased, the size of the trailing drop increases such that the leading drop volume remains nearly constant and the trailing drop breaks up into still smaller drops until drop sizes are all smaller than the critical drop size. In other words, a large drop tends to produce mono-dispersed drops through series of breakups. The conditions for a drop breakup are also investigated. In general, the critical drop size decreases with increasing values of the constriction parameter α; and for a fixed α, the critical drop size decreases with the Bond number. If the constriction is too severe and Bond number is not sufficiently large to force the drop through the constriction, the drop gets stuck at a throat and hydrostatic conditions are established eventually. It is shown that a breakup occurs the most effectively in moderately constricted channels. The critical capillary number is found to be independent of the constriction parameter at small Bond numbers, i.e., $Bo < 6$ and it is increasingly influenced by the constrictions as the Bond number increases. It is also observed that the critical capillary number gets smaller as the channel constriction increases. Effects of soluble surfactant on the dynamics of viscous drops is also investigated. It is found that increasing initial coverage value does not

effect the average rise velocity of small drops, whereas it can have an increase by up to 50 % for the average rise velocity of large drops, i.e., $\kappa > 0.80$. It is observed that surfactant is swept away to the trailing end of the drop where it accumulates and decreases the surface tension. This results in tail-streaming and breakup of small drops from the tail. Generally surfactants increases breakup and tail-streaming. It is also found that surfactants can decrease the nondimensional critical drop size for the onset of breakup considerably.

BIBLIOGRAPHY

[1] D.A. Caughey, "Diagonal implicit multigrid algorithm for the Euler equations," *AIAA J.*, vol. 26, pp. 841–851, 1988.

[2] R.M. Beam and R.F. Warming, "An implicit factored scheme for the compressible Navier-Stokes equations," *AIAA J.*, vol. 16, pp. 393–402, 1978.

[3] L. Fauci and S. Gueron, Eds. *Computational modeling in biological fluid dynamics*, Springer-Verlag, New York, 2001.

[4] M. Hemmat, "The motion of drops and bubbles through sinusoidally constricted capillaries," *Ph.D. Thesis*, The Pennsylvania State University, (1996).

[5] M. Hemmat and A. Borhan, "Buoyancy-driven motion of drops and bubbles in a periodically constricted capillary," *Chem. Eng. Commun.*, vol. 150, pp. 363–384, 1996.

[6] W.L. Olbricht and L.G. Leal, "The creeping motion of immiscible drops through a converging/diverging tube," *J. Fluid Mech.*, vol. 134, pp. 329–355, 1983.

[7] W.L. Olbricht, "Pore-scale prototypes of multiphase flow in porous media," *Annu. Rev. Fluid Mech.*, vol. 28, pp. 187–213, 1996.

[8] C. Peskin, "Numerical analysis of blood flow in the heart," *J. Comput. Phys.*, vol. 25, pp. 220–252, 1977.

[9] C. Pozrikidis, Ed. *Modeling and simulation of capsules and biological cells*, Chapman&Hall/CRC, 2003.

[10] H.A. Stone, A.D. Stroock and A. Ajdary, "Engineering flows in small devices: Microfluidics toward lab-on-a-chip," *Annu. Rev. Fluid Mech.*, vol. 36, pp. 381–411, 2004.

[11] G. Tryggvason, B. Bunner, A. Esmaeeli, D. Juric, N. Al-Rawahi, W. Tauber, J. Han, S. Nas and Y.-J. Jan, "A Front-Tracking Method for the Computations of Multiphase Flow," *J. Comput. Phys.*, vol. 169(2), pp. 708–759, 2001.

[12] T.M. Tsai, M.J. Miksis, "Dynamics of a droplet in a constricted capillary tube," *J. Fluid Mech.*, vol. 274, pp. 197–217, 1994.

[13] S.O. Unverdi and G. Tryggvason, "A front-tracking method for viscous incompressible multiphase flows," *J. Comput. Phys.*, vol. 100, pp. 25–37, 1992.

[14] A. Borhan and J. Pallinti, "Buoyancy-driven motion of viscous drops through cylindrical capillaries at small Reynolds numbers," *Ind. Eng. Chem. Res.*, vol 34, pp. 2750-2761 (1995).

[15] A. Borhan and J. Pallinti, "Breakup of drops and bubbles translating through cylindrical capillaries," *Phys. Fluids*, vol. 11(10), pp. 2846-2855 (1999).

[16] P.A. Gauglitz and C.J. Radke, "The dynamics of liquid film breakup in constricted cylindrical capillaries," *J. Colloid Interface Sci.*, vol. 134, pp. 14-40 (1990).

[17] E. Almatroushi and A. Borhan, "Surfactant effect on the buoyancy-driven motion of bubbles and drops in a tube," *Ann. N.Y. Acad. Sci.*, vol. 1027, pp. 330-341 (2004)

[18] B.P. Ho and L.G. Leal, "The creeping motion of liquid drops through a circular tube of comparable diameter," *J. Fluid Mech.*, vol. 71, 361-382 (1975).

[19] R.G. Larson, H.T. Davis and L.E. Scriven, "Displacement of residual nonwetting fluid from porous media," *Chem. Eng. Sci.*, vol 36, pp. 75-93 (1981).

[20] M. Muradoglu and S. Gokaltun, "Implicit multigrid computations of buoyant light drops through sinusoidal constrictions," *ASME J. Appl. Mech.*, vol 71(6), pp. 857-865, (2004).

[21] M. Muradoglu and A.D. Kayaalp, "An auxiliary grid method for computations of multiphase flows in complex geometries," *J. Comput. Phys.* **submitted**, (2005).

[22] H.A. Stone, "Dynamics of drop deformation and breakup in viscous fluids," *Annu. Rev. Fluid Mech.*, vol. 26, pp. 65-102 (1994).

[23] H.A. Stone and L.G. Leal, "The effects of surfactants on drop deformation and breakup," *J. Fluid Mech.*, vol. 220, pp. 161-186 (1989)

[24] W.J. Milleken,H.A. Stone and L.G. Leal, "The effect of surfactant on transient motion of newtonian drops," *Phys. Fluids A*, vol. 5, pp. 69-79 (1993)

[25] C.D. Eggleton, T.M. Tsai and K.J. Stebe, "Tip-streaming from a drop in the presence of surfactants," *Phys. Rev. Lett.*, vol. 87.048302 (2001)

[26] T.M. Tsai and M.J. Miksis, "The effects of surfactant on the dynamics of bubble snap-off," *J. Fluid Mech.*, vol. 337, pp. 381-410 (1997).

[27] H. Westborg and O. Hassager, "Creeping motion of long bubbles and drops in capillary tubes," *J. Colloid Interface Sci.*, vol.133, pp. 135-156 (1989).

[28] J.G. Roof, "Snap-off of oil droplets in water-wet pores," *Soc. Petrol. Engng. J.*, vol. 10, (1970)

[29] J. Lee and C. Pozrikidis, "Effects of surfactants on the deformation of drops and bubbles in navier-stokes flow," *Comp. and Fluids*, vol. 35(1), pp. 43-60 (2006)

[30] V.G. Levich and V.S. Krylov, "Surface-tension-driven phenomena," *Annu. Rev. Fluid Mech.*, vol. 1, pp. 293-316 (1958)

[31] H.A. Stone, "A simple derivation of the time-dependent convective-diffusion equation for surfactant transport along a deforming interface," *Phys. Fluids A*, vol. 2, pp. 111-112 (1990)

[32] A.J. James and J. Lowengrup, "A surfactant-conserving volume-of-fluid method for interfacial flows with insoluble surfactants," *J. Comp. Phys.*, vol. 201, pp. 685-722 (2004)

[33] C.D. Eggleton and K.J. Stebe, "An adsorption-desorption controlled surfactant on a deforming droplet," *J. Coll. Int. Sci.*, vol. 208, pp. 68-80 (1998)

VITA

Ufuk Olgaç was born in Istanbul, Turkey on November 1, 1980. He received the B. Sc. degree in Mechanical Engineering from Middle East Technical University, Ankara, in 2003. In October 2003, he joined the Mechanical Engineering Department of Koç University, Istanbul, Turkey as a teaching and research assistant and had studied for the *"Dynamics of Buoyancy-Driven Viscous Drops in Constricted Capillaries Including Effects of Soluble Surfactants"* project since October 2003.